Journal of Catalysis 287 (2012) 13–29

Contents lists available at SciVerse ScienceDirect

Journal of Catalysis

journal homepage: www.elsevier.com/locate/jcat

The catalysts of three-dimensionally ordered macroporous $Ce_{1-x}Zr_xO_2$-supported gold nanoparticles for soot combustion: The metal–support interaction

Yuechang Wei, Jian Liu, Zhen Zhao *, Aijun Duan, Guiyuan Jiang

State Key Laboratory of Heavy Oil Processing, China University of Petroleum, 18# Fuxue Road, Chang Ping, Beijing 102249, China

ARTICLE INFO

Article history:
Received 1 October 2011
Revised 5 November 2011
Accepted 7 November 2011
Available online 30 December 2011

Keywords:
Three-dimensionally ordered macroporous materials
Gold
$Ce_{1-x}Zr_xO_2$
Soot combustion
Heterogeneous catalysis
Interaction

ABSTRACT

Three-dimensionally ordered macroporous (3DOM) $Ce_{1-x}Zr_xO_2$-supported gold nanoparticle catalysts were successfully synthesized by the gas bubbling-assisted membrane reduction (GBMR) method. Au nanoparticles with similar sizes are well dispersed and supported on the inner walls of uniform macropores. The active oxygen species (O_2^-, O^-) over 3DOM Au/$Ce_{1-x}Zr_xO_2$ catalysts are derived from the two approaches: one is direct activation of oxygen on the surface of gold nanoparticles and the other is derived from strong metal–support interaction in which Ce-based supports serve as a reservoir for oxygen in the oxidation reaction. 3DOM Au/$Ce_{1-x}Zr_xO_2$ catalysts exhibited good catalytic performance for soot combustion, which is strongly related to the role of supports including the structures, the Ce/Zr ratios and the active oxygen supply pathways. The reaction pathways of soot combustion can be classified by two regions. At the low temperature, the soot particles are direct oxidized by active oxygen species migrated from the surface of supported Au catalysts. At the relatively high temperature, the catalytic activity for soot combustion is strongly related to intermediate reactant of NO_2 derived from NO oxidation.

1. Introduction

Diesel engines are prevalent power sources for vehicles owing to their efficient energy conversion, superior fuel economy and low CO_2 emissions, although they present the environmental drawbacks of particulate matter (PM, mainly containing soot) and NO_x formations as combustion by-products. The combination of traps and oxidation catalysts in the continuously regenerating particulate trap (CRT) appears to be one of the most efficient and economic after-treatment techniques [1]. The key challenge is to find a catalyst that can lower down the combustion temperature of soot as much as possible. Recently, several kinds of catalysts such as precious metals [2], transition metal oxides [3], alkaline metal oxides [4], perovskite-like type oxides [5] and ceria-based oxides [6] have exhibited good catalytic performances for diesel soot combustion. Especially, $Ce_{1-x}Zr_xO_2$ solid solutions are one of the key components in TWCs due to their excellent redox property, oxygen storage and releasing capacity and thermal stability [7]. In generally, catalytic approach of soot combustion is affected by two factors: the contact condition between soot and catalyst, and the intrinsic activity of catalyst. The conventional catalysts have smaller pore sizes (<10 nm) than soot particles (>20 nm). Thus, soot particles are difficult to enter the inner pores of these catalysts. The process of catalytic soot combustion is limited due to the poor soot/catalyst contact and the restricted active site amounts. So how to effectively make use of the inner surface for increasing the contact area between catalysts and soot particles is a key factor affecting the catalytic activity in heterogeneous catalysis reaction. In view of the catalytic combustion of diesel soot, controlling the porosity of catalysts is highly desirable. Three-dimensionally ordered macroporous (3DOM) perovskite or $Ce_{1-x}Zr_xO_2$ oxide catalysts [8,9] exhibited better catalytic performance for diesel soot oxidation in comparison with disordered macroporous and nanoparticles samples. The big pore sizes (>100 nm) can permit solid reactant to enter the inner pores of materials and to easily transport and diffuse. Consequently, the tangible active points between soot particles and catalysts will be increased dramatically. However, the catalytic performances of $Ce_{1-x}Zr_xO_2$ solid solutions are limited by their intrinsic activity. It is generally known that the addition of metal (active site) to oxides can modify the intrinsic catalytic properties of themselves due to the establishment of an interaction between metal and support, which can enhance the redox properties of the modified materials [10].

Since the pioneering studies by Haruta et al. [11] and Hutchings [12], supported gold catalysts have become one of the most extensively research issues in the field of heterogeneous catalysis [13,14]. Most of the studies have been focusing on the origin of

* Corresponding author. Fax: +86 10 89731586 (O).
E-mail address: zhenzhao@cup.edu.cn (Z. Zhao).

0021-9517/$ - see front matter © 2011 Elsevier Inc. All rights reserved.
doi:10.1016/j.jcat.2011.11.006

the unique catalytic activity of gold nanoparticles. The reasons are that, on the one hand, it is of great scientific interest accounting for chemical inert gold being changed to highly active materials. On the other hand, it may support the development of new catalysts in different fields such as low-temperature CO oxidation, selective catalytic oxidation and water gas shift reaction, and so on [15,16]. The efficiency of supported Au nanoparticles in a low-temperature reaction depends on the variety of factors, including the size and shape of Au particles [17], the role of the support [18], the oxidation state of the active gold species (metallic, Au^+ or Au^{3+}) [19], the cluster-support interactions, the oxygen supply pathways [20], the preparation procedures and pretreatment conditions [21]. It is commonly accepted that activation of O_2 is the most critical step in catalytic oxidation reactions involving gold. The reactivity of gold clusters with O_2 is important for understanding the remarkable catalytic effects. A critical question pertaining to the gold catalyst is how gold nanoparticles interact with and activate molecular oxygen in reactant gas. Among the commonly reported reasons of the chemisorption and activation of O_2 on Au-based catalysts are the so-called metal and support interactions, that is, specific phenomena occurring at the interface between the active metal phase (Au) and the support. Many ideas have been proposed in the catalysis literature on the origin of such support effects. These include electronic interactions between both components [22], stabilization or destabilization of certain particle shapes or sizes [23], surface transportation of adsorbates through the boundary (spillover, reverse spillover, capture zone effects) [24], so-called strong metal–support interactions involving migration of partially reduced oxides onto the active phase [25] or the stabilization/destabilization of oxidized active phases by the support [26]. However, the clear understanding for the effect of supports on catalyst performance is difficult due to interference with size effect in the wide size distribution of gold nanoparticles obtained by the conventional methods [27]. Up to date, an exact mechanism of gold catalysts has not been fully revealed, especially reaction mechanism for the reaction containing solid reactant is very rare.

Motivated by the above considerations, 3DOM $Ce_{1-x}Zr_xO_2$-supported gold catalysts as a bifunctional material, which combine both advantages of good contact between diesel soot and catalyst by 3DOM supports and the highly active sites for the activation of O_2 by gold clusters with suitable nanosize, are designed and they exhibit good catalytic performances for soot oxidation. The nature of an interaction between supports and gold nanoparticles and even its effect on the catalytic performance for soot combustion are investigated. Moreover, the possible mechanism for soot combustion over 3DOM Au/$Ce_{1-x}Zr_xO_2$ catalysts is proposed.

2. Experimental

2.1. Preparation of 3DOM $Ce_{1-x}Zr_xO_2$ solid solution supports

Synthesis of monodispersed PMMA microsphere, assembly template and preparation of 3DOM $Ce_{1-x}Zr_xO_2$ solid solution supports by colloidal crystal template (CCT) method are similar to that described previously [28]. The typical schematic diagrams are shown in Fig. S1. The dried sample was calcined to remove the CCT in a tube furnace with an air flow (80 ml min^{-1}). The temperature-rising rate was 1 °C min^{-1} from room temperature to 550 °C, and the calcination at 550 °C was kept for 5 h, and 3DOM $Ce_{1-x}Zr_xO_2$ solid solutions were obtained.

To compare the catalytic activity for soot combustion over different types of catalysts, the nano-$Ce_{1-x}Zr_xO_2$ solid solution catalysts were prepared by the micropore-diffused coprecipitation method with the ammonia solution as a precipitation agent and with various metal nitrates ($Ce(NO_3)_3{\cdot}6H_2O$ and $Zr(NO_3)_4{\cdot}3H_2O$) as precursors. The preparation method was described in literature [29].

2.2. Preparation of 3DOM $Ce_{1-x}Zr_xO_2$-supported gold nanoparticle catalysts

The synthesis of 3DOM Au/$Ce_{1-x}Zr_xO_2$ catalysts was carried out via the gas bubbling-assisted membrane reduction (GBMR) method which was just developed in our laboratory [30]. The catalysts will be generically named as 3DOM Au/$Ce_{1-x}Zr_xO_2$, where the weight percent of gold in the catalyst in theory is 2 wt%, and x is the molar ratio of Zr in $Ce_{1-x}Zr_xO_2$ solid solution. The schematic diagram of the GBMR method is presented in Fig. S2. The detailed synthesis mechanism of 3DOM $Ce_{1-x}Zr_xO_2$-supported gold nanoparticle catalysts is shown in Electronic Supportiong Informantion Section, and the schematic diagram of synthesis mechanism is presented in Fig. S3. The typical preparative procedures were described as follows: The poly (N-vinyl-2-pyrrolidone) (PVP) solution as a stabilizer was added into $HAuCl_4$ solution, which the [PVP]/[Au] ratio is 100. Then 3DOM $Ce_{1-x}Zr_xO_2$ support (0.5 g) was also introduced into the solution (50 ml). The mixture solution was driven by a peristaltic pump (Baoding Lange Co., Ltd.) and the rotate speed at 200 rpm (~360 ml min^{-1}) to form a tubal cycling flow. A reductant solution ($NaBH_4$) (1 ml min^{-1}, 50 ml) was injected into the membrane reactor with two ceramic membrane tubes (Φ 3 mm × 160 mm, Hyflux Group of Companies, Singapore) by a constant flow pump (HLB-2020, Satellite Manufactory of Beijing). Meantime, the hydrogen gas was also flow through the membrane rector with the other two membrane tubes. The metal precursor solution flowed inside the glass tube reactor and outside the ceramic tubes. The $NaBH_4$ solution was infiltrated through the abundant holes (d = 40 nm) on the wall of the ceramic tubes into the glass tube reactor, where the reduction in metal ions occurred immediately when the two solutions met. The hydrogen bubbling-assisted stirring operation (40 ml min^{-1}) was developed to vigorously stir the solution and to make the reaction homogenous. The synthesis process was stopped after complete consumption of the $NaBH_4$ solution. The reaction system was further vigorously bubbled with hydrogen gas for 1 h and then kept static for 1 h. Then, the product was filtered and washed with distilled water at 60 °C until the Cl^- was completely removed according to a test with $AgNO_3$, and the final products were dried in an oven at 200 °C for 1 h and the desired 3DOM Au/$Ce_{1-x}Zr_xO_2$ catalysts were obtained.

2.3. Physical and chemical characterization

The Brunauer–Emmett–Teller (BET) method was used to measure the specific surface areas of the samples. Mercury porosimetry experiments were carried out on a Micromeritics AutoPoreIV 9500 apparatus in the pressure range 0–30,000 psia. XRD patterns were measured on a powder X-ray diffractometer (Shimadzu XRD 6000) using Cu Kα (λ = 0.15406 nm) radiation with a Nickel filter operating at 40 kV and 10 mA in the 2θ range of 20–80° at a scanning rate of 4°/min. The patterns were compared with JCPDS reference data for phase identification. The crystallite sizes of obtained samples were calculated from the width of the (1 1 1) line using the Scherrer equation ($D = 0.9\lambda/(\beta\cos\theta)$, where λ is the wavelength of the radiation, β is the corrected peak width at half-maximum intensity (FWHM) and θ is the peak position). The UV–Vis diffuse reflectance spectroscopy (UV–Vis DRS) experiments were performed on a UV–Vis spectrophotometer (Hitachi U-4100) with the integration sphere diffuse reflectance attachment. The actual content of Au in catalysts was determined by inductive coupled plasma atomic emission spectrometry (ICP-AES)

(PE, OPTIMA 5300DV). The surface morphology of the catalyst was observed by field emission scanning electron microscopy (FESEM) on a Quanta 200F instruments using accelerating voltages of 5 kV. Samples for SEM were dusted on an adhesive conductive carbon belt attached to a copper disk and were coated with 10 nm Au prior to measurement. The TEM and HRTEM images were carried out using a JEOl JEM 2100 electron microscope equipped with a field emission source at an accelerating voltage of 200 kV. The average particle diameter was calculated from the mean diameter frequency distribution with the formula: $d = \sum n_i d_i / \sum n_i$, where n_i is the number of particles with particle diameter d_i in a certain range. Raman spectra of the samples were collected in the anti-Stokes range of 100–2000 cm^{-1} using a Jobin Yvon LabRam-HR spectrometer (HR800). The sample has been excited using a He–Gd laser (excitation wavelength of 325 nm). X-ray photoelectron spectra (XPS) were recorded on a Perkin–Elmer PHI-1600 ESCA spectrometer using Mg Ka ($h\nu$ = 1253.6 eV, 1 eV = 1.603×10^{-19} J) X-ray source. The binding energies were calibrated using C1s peak of contaminant carbon (BE = 284.6 eV) as an internal standard.

Fourier transform infrared spectroscopy (FT-IR) absorbance spectra were recorded in the wave numbers ranging from 6000 to 400 cm^{-1} via a FTS-3000 spectrophotometer manufactured by American Digilab company. The measured wafer was prepared as KBr pellet with the weight ratio of sample to KBr, 1/100. The resolution was set at 2 cm^{-1} during measurements. For in situ diffuse reflection infrared Fourier transformed (DRIFT) experiments, it did not need to use KBr as diluent. The spectra were recorded in the range of 600–4000 cm^{-1} after 256 scans at a resolution of 4 cm^{-1}. The powder sample was placed in a sample holder assembly in a Harrick Praying Mantis DRIFT cell. The gases were supplied by individual mass flow controllers with a total flow rate of 50 ml/min. Before reactant gases entering, the sample was pretreated with Ar at 300 °C for 30 min. The sample was then cooled to reaction temperature and equilibrated in Ar. After the sample had cooled to the reaction temperature, a spectrum of the treated sample was taken as the background at that temperature. The in situ experiment was performed by the introduction of 2000 ppm NO and 5% O_2 in Ar. Meanwhile, the IR spectra were sequentially recorded at the different reaction temperatures of 30 °C, 100 °C, 150 °C, 200 °C, 250 °C, 300 °C, 350 °C, 400 °C, and 450 °C, respectively. Temperature-programmed reduction with H_2 (H_2–TPR) measurements were performed in a conventional flow apparatus. 100 mg sample was pretreated under air atmosphere by calcination at 200 °C for 1 h and subsequently cooled to 30 °C. Afterwards, 10% H_2/Ar flow (40 ml/min) was passed over the catalyst bed while the temperature was ramped from 30 to 900 °C at a heating rate of 10 °C/min. The hydrogen consumption signal was monitored by a thermal conductivity detector (TCD). Before the outlet gases entering the TCD, a cooling trap and a filter packed with molecular sieve 5A (60–80 meshes) were used to remove H_2O and CO_2. To quantify the total amount of H_2 consumed during these experiments, CuO was used as a calibration reference. O_2–TPD measurements were performed on a conventional flow apparatus. 100 mg catalyst was pretreated in the Ar flow at 200 °C for 1 h. Then the catalyst was adsorbed O_2 for 30 min (40 ml min^{-1}) at room temperature and purged residual oxygen. The catalyst was heated to 900 °C at 10 °C min^{-1} rate under Ar flow (40 ml min^{-1}). The desorbed oxygen was monitored by TCD. NO temperature-programmed oxidation (TPO) experiments were performed on the above fixed beds for studying on the formation of NO_2. Reactant gas compositions were 5% O_2 and 0.2% NO with He balanced gas. The reaction temperature ranged from 100 °C to 500 °C. The catalyst used was 100 mg and without soot during the reaction. The other reaction conditions were the same as the following TPO experiment. The NO_2 concentration in the outlet gas was in situ detected by mass spectrometry (MS, Quantachrome autosorb-1C).

2.4. Activity measurements

The catalytic performances of all the catalysts were evaluated with a temperature-programmed oxidation reaction (TPO) on a fixed-bed tubular quartz reactor (ϕ = 8 mm), and each TPO run from 150 to 650 °C at a 2 °C min^{-1} rate. The model soot was Printex-U (diameter 25 nm, purchased from Degussa) as shown in Fig. S4. Elemental analysis of Printex-U particulates showed its carbonaceous nature with 92.0% C, 0.7% H, 3.5% O, 0.1% N, 0.2% S and 3.5% other [31]. The catalyst (100 mg) and soot (10 mg) were mixed at a weight ratio of 10:1 with a spatula in order to reproduce the loose contact mode. Reactant gases (50 ml min^{-1}) contain 5% O_2 and 0.2% NO balanced with Ar. The outlet gas compositions were analyzed with an on-line gas chromatograph (GC, Sp-3420, Beijing) by using FID detectors. Before entering the FID detector, CO and CO_2 were fully converted to CH_4 by a convertor with Ni catalyst at 380 °C. The catalytic activity was evaluated by the values of T_{10}, T_{50} and T_{90}, which were defined as the temperatures at 10%, 50% and 90% of soot conversion, respectively, were oxidized during the TPO procedure. The selectivity to CO_2 formation (S_{CO2}) was defined as that the CO_2 outlet concentration (C_{CO2}) divided by the sum of the CO_2 and CO outlet concentration, i.e., $S_{CO2} = C_{CO2}/(C_{CO} + C_{CO2})$. S^m_{CO2} was denoted as S_{CO2} at the maximum temperature corresponding to the soot-burnt rate was the highest. In all TPO experiments, the reaction was not finished until the soot was completely burnt off.

The turnover frequency (TOF) is defined as the ratio of reaction rate to the active site density of catalysts. The isothermal reactions for soot combustion were conducted for obtaining TOF value of catalyst, at which a stable and small conversion of soot was achieved in an approximate kinetic regime. The temperatures were selected at 210 °C and 300 °C because the soot conversion is low and the rate of soot conversion is nearly constant over time. Furthermore, a series of experiments were performed to exclude internal and external diffusion and heat transfer. The uniform macroporous structure and the small particle diameter (<40 μm) of catalysts could exclude the intraparticle mass transport limitations. Thus, the reaction rate and the TOF values of soot combustion can be obtained. Therein, TOF_{Au} is on the basis of Au loading amount determined by ICP-AES. The total flow rate was 50 ml/min, and reaction gas composition was same as the TPO reaction.

3. Results

3.1. Catalyst characterization

3.1.1. The results of SEM

The morphology and macroporous structure of all samples were investigated by the means of field emission scanning electron microscope (FESEM). Fig. 1 shows SEM images of 3DOM $Ce_{1-x}Zr_xO_2$ solid solutions obtained by colloidal crystal template method and $Au/Ce_{1-x}Zr_xO_2$ catalysts (x = 0–1) obtained by GBMR method. The images exhibit that the macroporous materials contain skeleton surrounding uniform close-packed periodic voids with the average diameter of 250 ± 20 nm, which corresponds to shrinkage of 25–30% compared with the initial size (350 nm) of PMMA microspheres (Fig. S5). This shrinkage is caused by the melting of polymer templates and sintering of the produced metal oxides. In addition, the wall thicknesses observed from SEM images are 30 ± 5 nm illustrates that the wall is composed of crystallite grains. The next layer is highly visible in the SEM image, and the voids are interconnected through the open window, ca. 65 ± 5 nm in

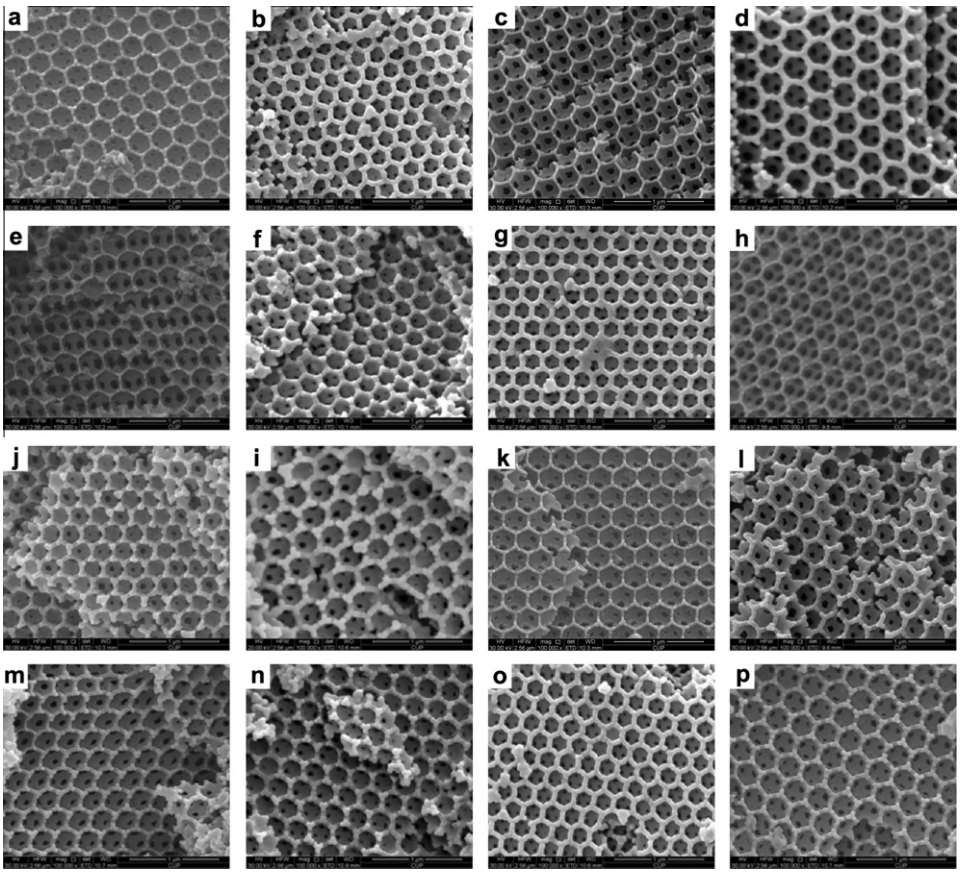

Fig. 1. SEM images of the 3DOM $Ce_{1-x}Zr_xO_2$ and $Au/Ce_{1-x}Zr_xO_2$ catalysts. (a) Au/CeO_2, (b) $Au/Ce_{0.9}Zr_{0.1}O_2$, (c) $Au/Ce_{0.8}Zr_{0.2}O_2$, (d) $Au/Ce_{0.7}Zr_{0.3}O_2$, (e) $Au/Ce_{0.6}Zr_{0.4}O_2$, (f) $Au/Ce_{0.5}Zr_{0.5}O_2$, (g) $Au/Ce_{0.3}Zr_{0.7}O_2$, (h) Au/ZrO_2, (i) CeO_2, (j) $Ce_{0.9}Zr_{0.1}O_2$, (k) $Ce_{0.8}Zr_{0.2}O_2$, (l) $Ce_{0.7}Zr_{0.3}O_2$, (m) $Ce_{0.6}Zr_{0.4}O_2$, (n) $Ce_{0.5}Zr_{0.5}O_2$, (o) $Ce_{0.3}Zr_{0.7}O_2$, (p) ZrO_2.

diameter. 3DOM $Au/Ce_{1-x}Zr_xO_2$ materials are similar to the well-defined 3DOM structure of $Ce_{1-x}Zr_xO_2$ supports obtained by colloidal crystal template method. It indicates that the synthesis process of GBMR method with gas bubbling-assisted stirring operation did not destroy the 3DOM structures.

3.1.2. The results of MIP and BET

The presence of macropores in the 3DOM catalysts was assessed by the means of mercury intrusion porosimetry (MIP). Fig. 2 displays the differential curves of pore size distribution of 3DOM $Ce_{1-x}Zr_xO_2$ and $Au/Ce_{1-x}Zr_xO_2$ catalysts (x = 0.2, 0.3) as representative examples. The diameter corresponding to the peak value of different curve is regarded as the most probable pore diameter, whose size occupies the largest proportion of pores compared with other pore diameters. The narrower the most probable pore diameter, the finer the pore structure. It can be seen in Fig. 2 that the macropores (those in the 30∼200 nm range) in this sample are very regular, and the most probable pore diameters of 3DOM catalysts do not obviously change after supporting gold nanoparticles, which is consistent with the observation that the open windows interconnected macropores in SEM images. The total specific pore volumes and the average pore diameters of various concretes are analyzed and compared, and the results are given in Table 1. The total pore volume of the materials determined by N_2 physisorption (∼0.07 ml g^{-1}) is less than 3% of the total pore volume (∼3.4 ml g^{-1}) determined by mercury porosimetry, indicating main contribution of macropores to the total porosity in these materials. The average pore diameter of 3DOM materials is about ∼260 nm, which is in good agreement with the results of SEM images. The porosity of 3DOM materials is beyond 90%, indicating that the solid reactants can easily diffuse in the materials. Therefore, 3DOM $Ce_{1-x}Zr_xO_2$ supported Au catalysts will have good catalytic performance for the catalytic combustion of solid particles.

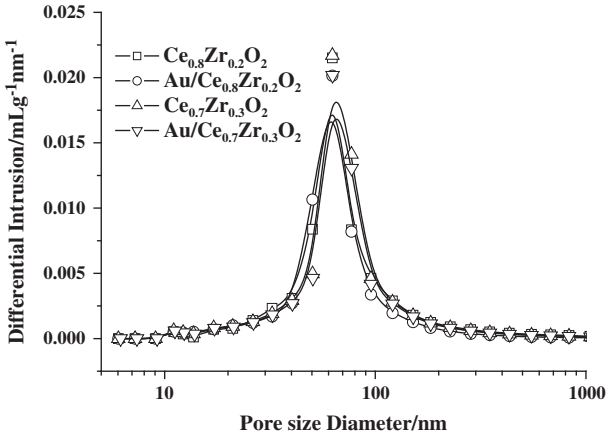

Fig. 2. Pore size distribution of the 3DOM $Ce_{1-x}Zr_xO_2$ and $Au/Ce_{1-x}Zr_xO_2$ (x = 0.2, 0.3) catalysts determined by MIP.

The BET surface areas of 3DOM $Ce_{1-x}Zr_xO_2$ solid solutions and $Au/Ce_{1-x}Zr_xO_2$ catalysts ($0 \leqslant x \leqslant 1$) are listed in Table 2. The BET surface areas of the 3DOM catalysts are 44–60 $m^2\ g^{-1}$. As shown in Table 2, no obvious changes of their BET surface areas are observed after Au nanoparticle deposited on the surface of 3DOM $Ce_{1-x}Zr_xO_2$ solid solutions. As shown in Fig. S6, no organic residues (PVP) over 3DOM $Au/Ce_{1-x}Zr_xO_2$ catalysts are detected by FT-IR spectra.

Table 1
Porosities, average diameters, pores volume and pore areas of 3DOM $Ce_{1-x}Zr_xO_2$ and $Au/Ce_{1-x}Zr_xO_2$ catalysts (x = 0.2, 0.3).

Catalyst	V_p[a] (ml g^{-1})	A_p[b] (m^2 g^{-1})	V_{Hg}[c] (ml g^{-1})	D_p[d] (nm)	Porosity[e] (%)
$Ce_{0.8}Zr_{0.2}O_2$	0.08	52.7	3.4	261	92.3
$Au/Ce_{0.8}Zr_{0.2}O_2$	0.07	50.6	3.3	259	92.0
$Ce_{0.7}Zr_{0.3}O_2$	0.07	54.4	3.7	265	92.8
$Au/Ce_{0.7}Zr_{0.3}O_2$	0.07	53.2	3.5	262	92.9

[a] Pore volume determined by BET method.
[b] Total pore area determined by MIP.
[c] Total pore volume for pores.
[d] The average pore diameters.
[e] Determined by Hg porosimetry.

Table 2
Average crystal parameters and crystal sizes of the 3DOM $Ce_{1-x}Zr_xO_2$ and $Au/Ce_{1-x}Zr_xO_2$ catalysts with different Au loading amounts.

Catalyst (3DOM)	D[a] (nm) ($Ce_{1-x}Zr_xO_2$)		S_{BET}[c] (m^2 g^{-1})		Au size[b] (nm)	Au content[d] (wt.%)
	Without Au	With Au	Without Au	With Au		
Au/CeO_2	13.1	13.1	60	62	3.4	1.3
$Au/Ce_{0.9}Zr_{0.1}O_2$	10.2	10.2	54	57	3.3	1.3
$Au/Ce_{0.8}Zr_{0.2}O_2$	8.9	8.8	56	57	3.3	1.5
$Au/Ce_{0.7}Zr_{0.3}O_2$	8.7	8.6	59	58	3.4	1.4
$Au/Ce_{0.6}Zr_{0.4}O_2$	9.3	9.3	51	53	3.2	1.3
$Au/Ce_{0.5}Zr_{0.5}O_2$	9.9	10.0	50	50	3.2	1.2
$Au/Ce_{0.3}Zr_{0.7}O_2$	11.7	11.7	47	49	3.2	1.3
Au/ZrO_2	21.7	21.7	44	44	3.2	1.2

[a] Determined by XRD using Scherrer equation with the intensity of the most prominent peak, (1 1 1).
[b] Determined by HRTEM.
[c] Surface area obtained by BET method.
[d] Determined by ICP-AES.

3.1.3. The results of XRD

To confirm the formation and phase structures of 3DOM $Ce_{1-x}Zr_xO_2$ solid solutions and $Au/Ce_{1-x}Zr_xO_2$ catalysts ($0 \leqslant x \leqslant 1$), XRD measurements were carried out and the XRD patterns are shown in Fig. 3. All the diffraction peaks of the 3DOM CeO_2 solid solution and Au/CeO_2 catalyst can be indexed to the (1 1 1), (2 0 0), (2 2 0), (3 1 1), (4 0 0) and (3 3 1) crystal faces, which correspond to a face centered cubic (FCC) fluorite structure of CeO_2 (JCPDS 43-1002).

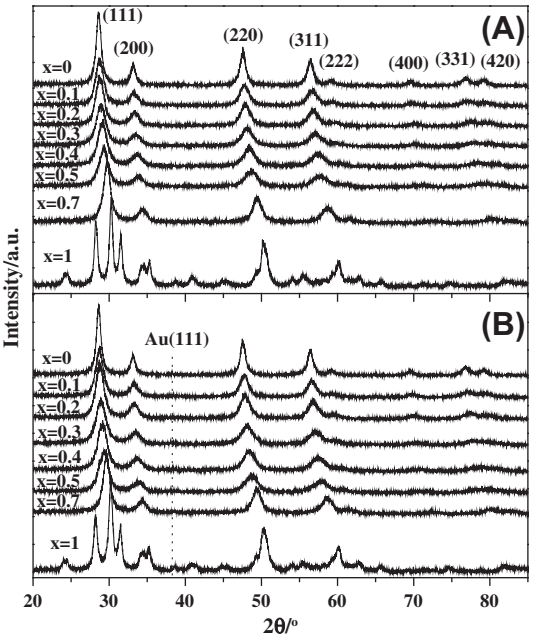

Fig. 3. XRD patterns of the 3DOM $Ce_{1-x}Zr_xO_2$ solid solutions (A) and $Au/Ce_{1-x}Zr_xO_2$ catalysts (B) ($0 \leqslant x \leqslant 1$).

For the 3DOM ZrO_2 and Au/ZrO_2 catalysts, all the diffraction peaks of XRD pattern indicate the coexistence of the two crystal phases structures including monoclinic (JCPDS 36-0420) and orthorhombic (JCPDS 37-1413). However, no ZrO_2 crystal phase was detected in all the XRD profiles of $Ce_{1-x}Zr_xO_2$ solid solutions ($x > 0$), which indicates the formation of solid solutions. With increasing of x in 3DOM $Ce_{1-x}Zr_xO_2$ solid solutions ($0 \leqslant x \leqslant 0.7$), the diffraction peaks of 2θ show a slight upshift from 28.8 to 30.0 °C. The effect is primarily due to Zr^{4+} ion entering into the fluorite-type lattice of ceria and forming $Ce_{1-x}Zr_xO_2$ solid solutions, leading to the shrinkage of the lattice. The peaks of the XRD patterns of 3DOM $Ce_{1-x}Zr_xO_2$ solid solutions and $Au/Ce_{1-x}Zr_xO_2$ catalysts are sharp for the sample with low ceria. As the ceria content increases, it becomes broad, attributing to the presence of the smaller average crystallite sizes of the $Ce_{1-x}Zr_xO_2$ solid solutions. As shown in Fig. 3B, no characteristic diffraction peaks (~38.1°) belonging to Au nanoparticles were detected after 3DOM $Ce_{1-x}Zr_xO_2$-supported gold nanoparticles, indicating the high dispersion and small size of Au particles on the surface of 3DOM $Ce_{1-x}Zr_xO_2$ solid solution supports. The average crystallite sizes of the 3DOM $Ce_{1-x}Zr_xO_2$ solid solutions are calculated by Scherrer equation using the intensity of the most prominent peak to (1 1 1) crystal face, and the calculated values are summarized in Table 2. The average crystallite size of the 3DOM $Ce_{0.7}Zr_{0.3}O_2$ solid solution shows that the smallest value is 8.7 nm, which is corresponding to ca. 3–4 crystallites per 3DOM $Ce_{0.7}Zr_{0.3}O_2$ solid solution wall thickness. No obvious changes of their crystallite sizes are observed after Au nanoparticle deposited on the surface of 3DOM $Ce_{1-x}Zr_xO_2$ solid solutions. Therefore, it can be concluded that the deposition of Au nanoparticles on the surface of 3DOM $Ce_{1-x}Zr_xO_2$ solid solutions leads to less impact on the crystalline phase, crystalline size and crystallinity of 3DOM $Ce_{1-x}Zr_xO_2$ solid solutions.

3.1.4. The results of TEM and HRTEM

Fig. 4 shows the TEM images of 3DOM $Ce_{1-x}Zr_xO_2$-supported Au nanoparticle catalysts with same Au loading amount of 2 wt.%. The

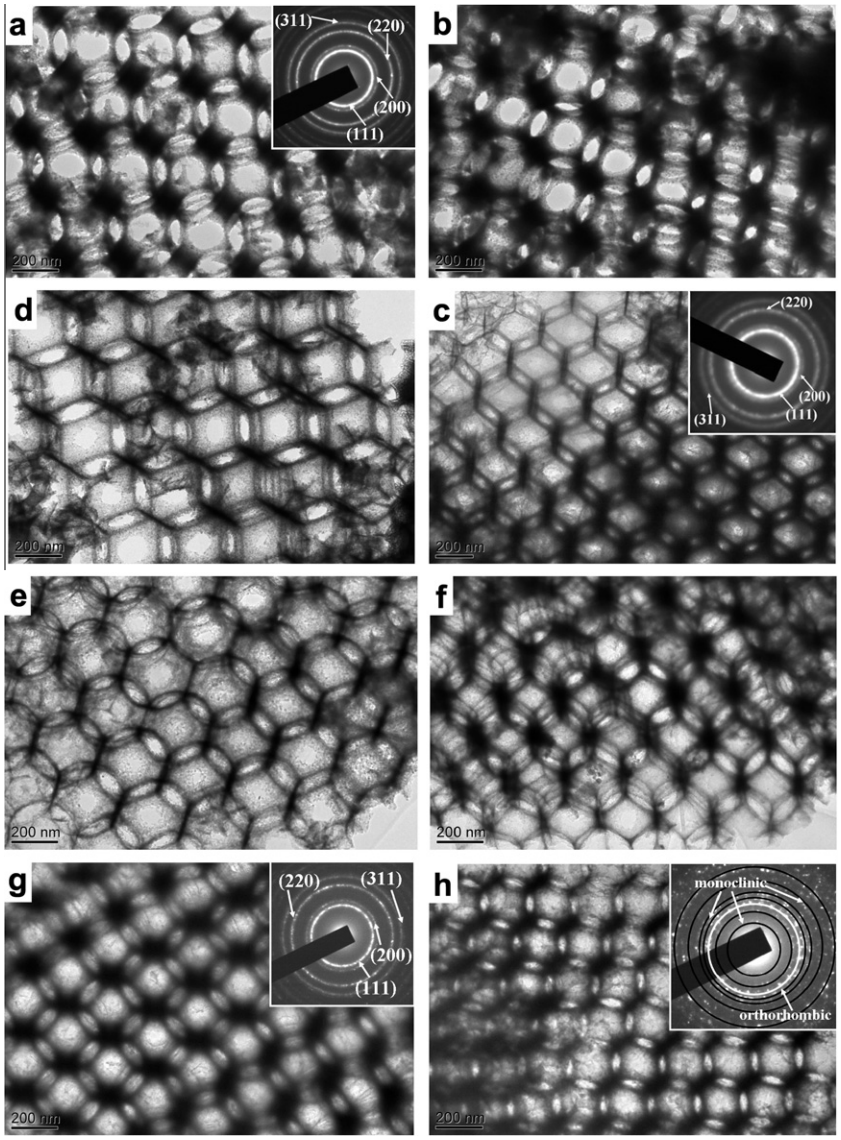

Fig. 4. TEM images of the 3DOM Au/$Ce_{1-x}Zr_xO_2$ catalysts. The ones in a, c, g, h images are the corresponding SAED pattern. (a) Au/CeO_2, (b) Au/$Ce_{0.9}Zr_{0.1}O_2$, (c) Au/$Ce_{0.8}Zr_{0.2}O_2$, (d) Au/$Ce_{0.7}Zr_{0.3}O_2$, (e) Au/$Ce_{0.6}Zr_{0.4}O_2$, (f) Au/$Ce_{0.5}Zr_{0.5}O_2$, (g) Au/$Ce_{0.3}Zr_{0.7}O_2$, (h) Au/ZrO_2.

3DOM structure with overlapped pores can be clearly observed by TEM images after the loading Au nanoparticles. The pore sizes of 3DOM $Ce_{1-x}Zr_xO_2$ supports are 250 ± 20 nm, and the voids are interconnected through open windows with 65 nm in diameter, which is in agreement with the observed by SEM images and MIP. The walls of the macroporous samples are crystalline by selected area electron diffraction (SAED) (inset in Fig. 4a, c, and g), which the characteristic SAED rings of the $Ce_{1-x}Zr_xO_2$ solid solutions except for ZrO_2 are indexed as (111), (200), (220) and (311) planes of face centered cubic (fcc) fluorite structure, and the SAED rings of ZrO_2 show the coexistence of the two crystal phase structures, which are in accord with the results of XRD characterization. The perfect macroporous structure provides the ideal reaction space for solid reactants (diesel soot, as shown in Fig. S4). The pore sizes of these catalysts are big enough to permit soot particles to enter their inner pores and reduce the diffusion resistance, and the number of contact points between soot and catalysts will be increased dramatically. Therefore, the catalytic activity for soot combustion over 3DOM catalysts will be enhanced remarkably.

Fig. 5 shows the HRTEM images and size distribution of Au nanoparticles over 3DOM $Ce_{1-x}Zr_xO_2$ solid solutions. The spherical gold nanoparticles precipitated on the surface of 3DOM $Ce_{1-x}Zr_xO_2$ supports can be clearly observed in HRTEM images, and all Au particles are highly dispersed and uniformed in size. The sizes of Au nanoparticles over 3DOM $Ce_{1-x}Zr_xO_2$ solid solutions are in the range of 1–6 nm with a narrow size distribution, and the mean diameters of Au nanoparticles for all catalysts are 3.3 ± 0.1 nm by statistic analysis of more than 300 Au particles for each sample. The lattice fringes of gold particles and $Ce_{1-x}Zr_xO_2$ solid solution particles in HRTEM images were clearly observed, for example the lattice fringes was measured to be 2.35 Å indexed as (111) planes of fcc gold particle in Fig. 5a and g. It indicates that supported Au particles are crystalline and exposed fcc (111) plane. The particle sizes of $Ce_{1-x}Zr_xO_2$ solid solutions ($x < 1$) are in the range of 5–15 nm, which is in accord with the result of XRD characterization. Supported Au nanoparticles exhibited hemispherical morphology on the surface of the $Ce_{1-x}Zr_xO_2$ supports, and the contact angle is about 90° in Fig. 5g. It is evident that the roughness originated from the contact between the Au nanoparticles and the $Ce_{1-x}Zr_xO_2$ supports, which is an indication of the existence of a strong metal–support interaction. The material of nanocomposite structure in Fig. 6b, between nanometric crystal of $Ce_{1-x}Zr_xO_2$ solid

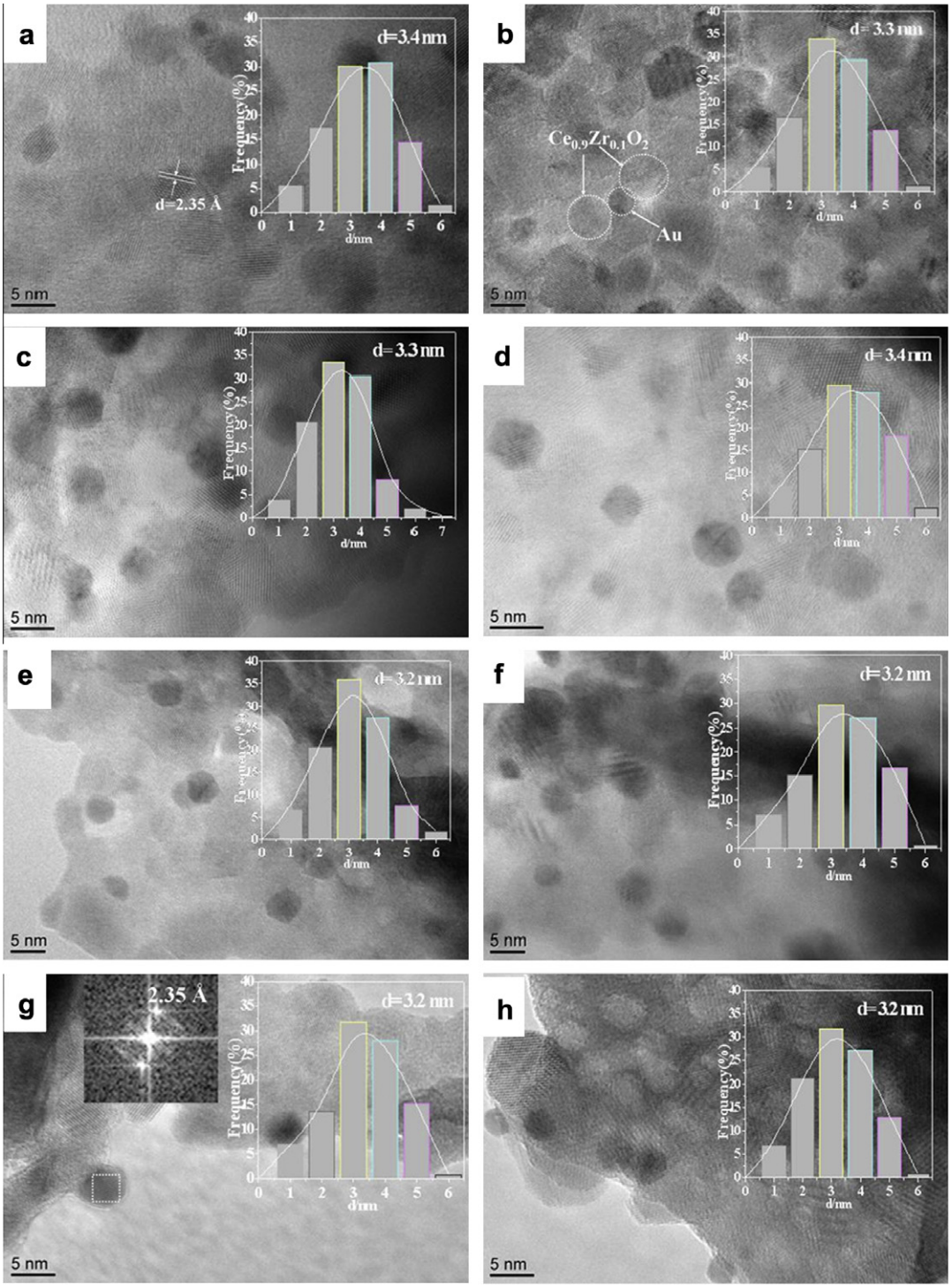

Fig. 5. The HRTEM images and size distribution of Au nanoparticles over 3DOM $Ce_{1-x}Zr_xO_2$ solid solutions. The lattice fringes in a image correspond to (1 1 1) plane of Au particle at 2.35 Å. The one in g image shows an Au particle whose lattice fringes correspond to fcc (1 1 1) plane at 2.35 Å in fast Fourier transform (FFT) image. (a) Au/CeO_2, (b) $Au/Ce_{0.9}Zr_{0.1}O_2$, (c) $Au/Ce_{0.8}Zr_{0.2}O_2$, (d) $Au/Ce_{0.7}Zr_{0.3}O_2$, (e) $Au/Ce_{0.6}Zr_{0.4}O_2$, (f) $Au/Ce_{0.5}Zr_{0.5}O_2$, (g) $Au/Ce_{0.3}Zr_{0.7}O_2$, (h) Au/ZrO_2.

solution supports (~8 nm) and Au nanoparticles active component (~3 nm), should possess strong synergetic effect for redox ability because the composite structure is favorable for the mobility of lattice oxygen in catalysts [32]. The particle size and physical structure of the gold nanoparticles are very similar in 3DOM $Au/Ce_{1-x}Zr_xO_2$ catalysts, indicating that the interference of size effect of Au particles may be ignored in the identification of the influence of the support on the catalytic activity.

3.1.5. The results of UV–Vis DRS

As a source of complementary information on the particle size of supported gold particles, UV–Vis DRS spectroscopy has been considered to be one of the most appropriate techniques due to the surface plasmon resonance (SPR) wavelength strongly depending on the size of supported Au nanoparticles [33]. The surface plasmon adsorption in the metal nanoparticles arises from the collective oscillations of the free conduction band electron induced by the

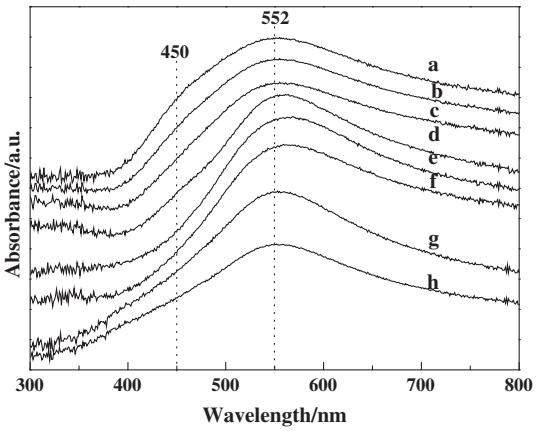

Fig. 6. The UV–Vis DRS spectra of 3DOM Au/$Ce_{1-x}Zr_xO_2$ catalysts recorded by using 3DOM $Ce_{1-x}Zr_xO_2$ solid solutions as reference samples. (a) Au/CeO_2, (b) Au/$Ce_{0.9}Zr_{0.1}O_2$, (c) Au/$Ce_{0.8}Zr_{0.2}O_2$, (d) Au/$Ce_{0.7}Zr_{0.3}O_2$, (e) Au/$Ce_{0.6}Zr_{0.4}O_2$, (f) Au/$Ce_{0.5}Zr_{0.5}O_2$, (g) Au/$Ce_{0.3}Zr_{0.7}O_2$, (h) Au/ZrO_2.

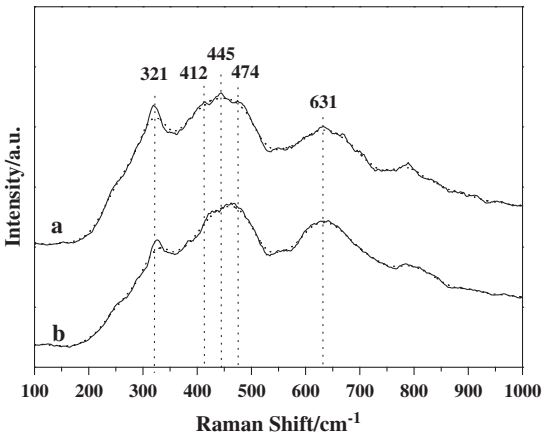

Fig. 7. Raman spectra of 3DOM $Ce_{0.8}Zr_{0.2}O_2$ (a) and Au/$Ce_{0.8}Zr_{0.2}O_2$ (b) catalysts.

incident electromagnetic radiation. Such resonances are seen when the wavelength of the incident light far exceeds the particle diameter. To verify the electronic state of the Au nanoparticles on the surface of 3DOM $Ce_{1-x}Zr_xO_2$ solid solution carriers, the UV–Vis DRS spectra of 3DOM Au/$Ce_{1-x}Zr_xO_2$ catalysts using 3DOM $Ce_{1-x}Zr_xO_2$ solid solutions as reference sample were recorded, and the results are shown in Fig. 6. The diffuse reflectance spectra of the supported Au nanoparticle catalysts display well-defined surface plasmon absorption band centered at ~552 nm with different catalysts, which is the characteristic of nanocrystalline Au particles (diameter <5 nm) and confirm the low degree of their polydispersity. [34] It is accord with the calculated results of HRTEM images on the size distribution of supported Au nanoparticles. Generally speaking, the decreasing in particle size causes the increase in quantization of surface plasmon oscillation, resulting in a blue shift of the plasmon band [35]. It is known that the frequency and the strength of the resonance were determined by the size and shape of the particles as well as the dielectric function of the surrounding medium. In this study, the position and shape of the plasmon absorption band of supported gold nanoparticles are slightly different as judged from the DRS data, which the shoulder peak intensity of the plasmon adsorption band at 450 nm decreased with the increasing of Zr-doped amount. It indicates that the 3DOM $Ce_{1-x}Zr_xO_2$ matrix has strong chemical interaction with the gold surface, and the strong interaction is related to the amount of Ce in supports. It was demonstrated from the above results that well-defined Au nanoparticles on the 3DOM $Ce_{1-x}Zr_xO_2$ support could be successfully fabricated through GBMR method.

3.1.6. The results of Raman spectroscopy

In contrast to the cation-dominated information yielded by XRD, Raman spectra of fluorite-related phases are dominated by lattice oxygen vibrations [36] and are obviously sensitive to the crystalline symmetry. Thus, it is a useful tool to obtain the additional structural information of both M–O bond arrangement and lattice defects [37]. The Raman spectra of 3DOM $Ce_{0.8}Zr_{0.2}O_2$ carrier and Au/$Ce_{0.8}Zr_{0.2}O_2$ catalyst are presented in Fig. 7. For 3DOM $Ce_{0.8}Zr_{0.2}O_2$ solid solution, there are three Raman bands located at ~321, ~445 and ~630 cm^{-1} in Fig. 7a. The appearance of weak band at ~321 cm^{-1} could be attributed to displacement of oxygen atoms from their ideal fluorite lattice position [38]. The broad and subtle band centered at ~445 cm^{-1} could be attributed to the symmetric stretching mode (F_{2g}) of the oxygen atoms around cerium ions [39]. The band at ca. 631 cm^{-1} corresponded to a doubly degenerate into longitudinal optical mode of CeO_2, and this band could be linked to oxygen vacancies due to the substitution of Zr^{4+} into the ceria lattice [40]. Compared with 3DOM $Ce_{0.8}Zr_{0.2}O_2$ catalyst, the Raman spectra of 3DOM Au/$Ce_{0.8}Zr_{0.2}O_2$ catalyst exhibits the significant difference between the curve (a) and (b). The strongest peak centered at 445 cm^{-1} shifts by 15 cm^{-1} toward the high wave number and the two shoulder peaks (412 and 474 cm^{-1}) disappeared suggests that a certain loss of anion-lattice ordering leads to the low symmetry of the oxygen atoms around cerium ions, because the interaction between Au atom and supports induces a localized defect or an impurity-derived vibration mode of lattice oxygen. In addition, the intensity of the peak at 631 cm^{-1} obviously increases could be ascribed to the change of amount of oxygen vacancies. Therefore, we can deduce that a strong metal–support interaction between Au atom and Ce atom may exist, which in accordance with the observations by HRTEM images and UV–Vis DRS, and the strong interaction is beneficial to the creation of the oxygen vacancies. The similar effect observed by Raman spectra has been reported in Pd/Ceria systems [41].

3.1.7. The results of H_2–TPR

For metal oxide catalysts, H_2–TPR measurement can simultaneously reflect the reducibility of metallic ion with high valence converting to the ion with low valence or metallic atom, and the potential to remove or take up oxygen, i.e., the mobility of the lattice oxygen (O^{2-}) [42]. Thus, the temperature of reduction peak (T_{red}) is taken as a measure to evaluate the redox ability of catalyst. The lower T_{red} is, the stronger is the redox ability of catalysts. Since the rate of soot oxidation at low temperature is more important than that of at high temperature in practical applications, we especially focus on the lowest T_{red} of H_2–TPR. The H_2–TPR curves of 3DOM $Ce_{1-x}Zr_xO_2$ solid solutions and Au/$Ce_{1-x}Zr_xO_2$ catalysts are shown in Fig. 8. As shown in Fig. 8A, there are two apparent reduction peaks ranging from 280 to 600 °C. The one reduction peak at low temperature (~350 °C) is attributed to the reduction of the adsorbed oxygen, and the other reduction peak (~503 °C) corresponds to the outermost layers reduction of Ce^{4+}–Ce^{3+}. The reduction peak ranging from 650 to 850 °C can be attributed to the reduction of the inner Ce^{4+} layer and lattice oxygen (bulk reduction). With the increasing of Zr-doped content, the peak at around 503 °C gradually shifts toward higher temperature and the reduction peak at high temperature becomes weak, which indicates the reduction of the reducibility of catalysts [43]. Among these catalysts, the consumption amount of H_2 for the peak ranging from 280 to 600 °C over $Ce_{0.8}Zr_{0.2}O_2$ catalyst is the largest

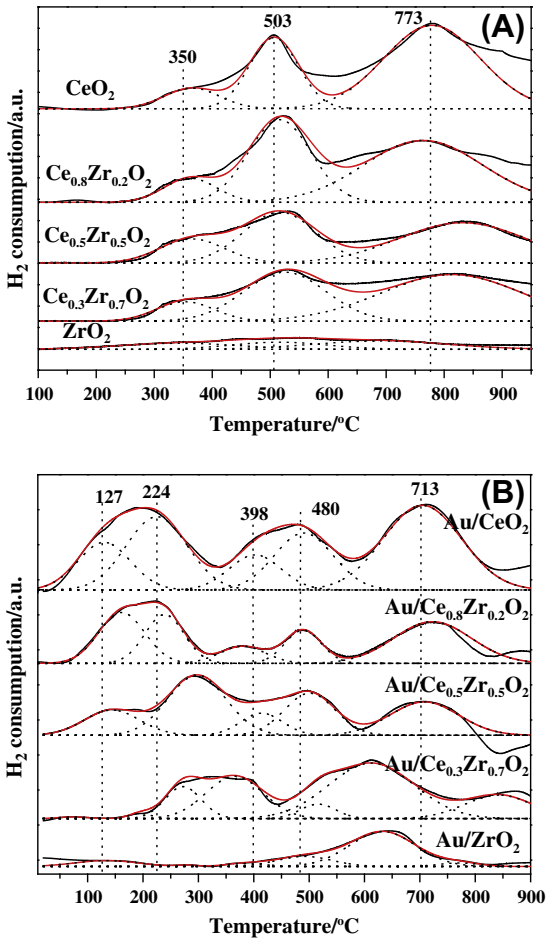

Fig. 8. The H_2–TPR profiles of 3DOM $Ce_{1-x}Zr_xO_2$ solid solutions (A) and Au/$Ce_{1-x}Zr_xO_2$ catalysts (B).

quantified by using CuO as a calibration reference (Table S1), which is attributed to the increasing reduction extent of supports with the moderate Zr-doped content into the ceria lattice.

As shown in Fig. 8B, the H_2–TPR profiles of 3DOM Au/$Ce_{1-x}Zr_xO_2$ catalysts are obviously different from those of 3DOM $Ce_{1-x}Zr_xO_2$ solid solutions. The profiles of 3DOM Au/$Ce_{1-x}Zr_xO_2$ catalysts show a series of strong peaks within the lower reduction temperatures ranging from 50 to 350 °C compared with 3DOM $Ce_{1-x}Zr_xO_2$ oxides. The result suggests that a strong interaction between nanogold particulates and supports occurs on 3DOM Au/$Ce_{1-x}Zr_xO_2$ catalysts [44]. They can be related to the reduction of the chemisorption's oxygen species on highly dispersion supported Au nanoparticles (Au–O_x to Au) or the interface between Au particles and supports (Ce–O_x–Au to Au), which is related to the weakening of the Ce–O bond induced by gold atom [45]. With the increasing of the Zr-doped content, the temperature of reduction peaks gradually shifts to the higher temperature from 224 to 360 °C. Even, the Au/ZrO_2 catalyst does not exhibit a clear reduction peak related to gold at the low reduction temperatures. This result indicates that the interaction between Au and Zr is not strong as that of Au and CeO_2. Among these catalysts, 3DOM Au/$Ce_{1-x}Zr_xO_2$ catalysts ($x \leqslant 0.2$) display better reacting behaviors toward H_2 oxidation at the lower temperatures due to the strong metal (Au)-support (Ce) interaction, indicating that they will give better catalytic performances for soot oxidation. Table S2 shows the amount of H_2 consumption for the each peak and the total five peaks with different temperatures and the total amounts for all the peaks on 3DOM Au/$Ce_{1-x}Zr_xO_2$ catalysts. It is noteworthy that the amount of H_2 consumption for the lowest temperature reduction peaks on 3DOM Au/$Ce_{0.8}Zr_{0.2}O_2$ catalyst is the largest, which is 41.5 μmol. However, the total amount of H_2 consumption at the lower temperatures decreases with the increasing of Zr-doped content, which can be assigned to the decreasing amount of surface oxygen species over the surface of catalysts. It indicates that the redox ability of catalyst is strongly related to the elements of Au and Ce. The surface reducible species of the gold oxide (AuO_x or $Au(CeO_2)_y$), which intimately interacted with the $Ce_{1-x}Zr_xO_2$ solid solutions, are formed by the diffusion of Au atoms into sublayers of $Ce_{1-x}Zr_xO_2$ solid solutions [46]. Therefore, the obtained results suggest that the different supports-surface composition can provide different reacting behaviors of Au toward H_2 oxidation and can enlighten different synergic effects between the 3DOM $Ce_{1-x}Zr_xO_2$ supports and Au nanoparticles [47].

3.1.8. The results of O_2–TPD

To further investigate the adsorption and activation of oxygen on carriers and supported Au catalysts, O_2–TPD measurements were carried out, and the results are displayed in Fig. 9. The O_2 desorption peaks of 3DOM $Ce_{1-x}Zr_xO_2$ carriers are relatively weak. The O_2–TPD profile of 3DOM $Ce_{0.8}Zr_{0.2}O_2$ solid solution shows that there are two desorption peaks of oxygen at 66 and 171 °C, which are assigned to the desorption of physical adsorption oxygen species (O_2) and chemisorption's oxygen species (O_2^-), respectively. It indicates that the desorption oxygen capability of $Ce_{1-x}Zr_xO_2$ solid solutions will be influenced by the doping Zr content. As shown in Fig. 9B, the O_2–TPD profiles of 3DOM Au/$Ce_{1-x}Zr_xO_2$ catalysts show that there are four oxygen desorption peaks centered at 92, 190,

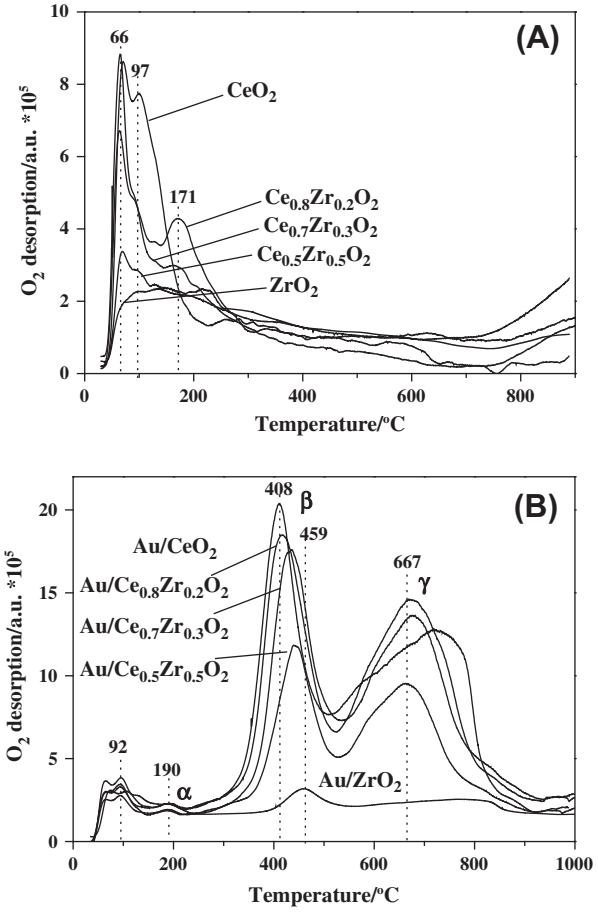

Fig. 9. The O_2–TPD curves of 3DOM $Ce_{1-x}Zr_xO_2$ solid solutions (A) and Au/$Ce_{1-x}Zr_xO_2$ catalysts (B).

408 and 667 °C. The first peak at lowest temperature is assigned to the desorption of physical adsorption oxygen species (O_2). The desorption peaks in the temperature range from 180 to 500 °C can be assigned to chemisorption's surface active oxygen species (O_2^-, O^-), and the peak at high temperature should be assigned to lattice oxygen (O^{2-}) [48]. Compared with $Ce_{1-x}Zr_xO_2$, it is clearly that the intensity of desorption peaks of physical adsorption oxygen species on $Au/Ce_{1-x}Zr_xO_2$ remarkably decrease, indicating that the interaction between adsorption oxygen and catalyst becomes strong after loading Au nanoparticles, and physical adsorption oxygen specie may convert into chemisorption oxygen species. The amount of surface active oxygen species over the catalysts decreases with the increasing of Zr-doped content, especially surface activated oxygen species (β) and lattice oxygen (γ). The analysis results of O_2–TPD in Table 3 show that the amounts of surface active oxygen species (O_2^-, O^-) over the catalysts are strongly depended on the nature of supports. The amount of active oxygen species (α) over 3DOM $Au/Ce_{0.8}Zr_{0.2}O_2$ catalyst is the largest, and the amounts of active oxygen species (β and γ) decrease with the increasing of doping Zr content, even no γ oxygen species for 3DOM Au/ZrO_2 catalyst was found. It indicated that there is the strong synergetic effect between Au nanoparticles and $Ce_{1-x}Zr_xO_2$ solid solutions, and the Ce/Zr ratio in 3DOM $Au/Ce_{1-x}Zr_xO_2$ catalysts is a critical factor for this interaction. Therefore, we deduce that a distribution of electronic charges between a small cluster of Au atom and support can weaken the Ce(Zr)–O bond, and the presence of gold increases the amount of surface oxygen in $Ce_{1-x}Zr_xO_2$ solid solutions. This increase can occur through partial occupation of vacant Ce sites with Au^+, which will create additional oxygen vacancies on the surface of the Ce^{4+}–O_2 fluorite-type oxide [49]. Consequently, the adsorption and activation of oxygen are dependent on the capacity to supply oxygen of support, especially the amount of surfaces active oxygen species (O_2^-, O^-) [25]. It is very consistent with the results of H_2–TPR characterization.

3.1.9. The results of XPS

The catalytic performance of materials for oxidation reaction is correlated with the capability to activate oxygen. How do the supported Au nanoparticle catalysts interact with surface oxygen species? To examine the electronic properties of the supported Au nanoparticles and surface oxygen species, 3DOM $Ce_{0.8}Zr_{0.2}O_2$ and $Au/Ce_{0.8}Zr_{0.2}O_2$ catalysts were studied by XPS, and the results are shown in Fig. 10. The XPS spectra in the Au 4f region of 3DOM $Au/Ce_{0.8}Zr_{0.2}O_2$ catalyst are shown in Fig. 10A. Deconvolution of the Au spectra indicates that both metallic and ionic gold species are present in supported Au nanoparticle catalysts, i.e., the gold species of metal (Au^0) and ion (Au^+ and Au^{3+}) are identified on the surface of catalysts [50]. The concentrations of Au^+ species measured by XPS are about 20.7 at.% (the atomic ratio of Au^+ to the total Au atoms) on the $Au/Ce_{0.8}Zr_{0.2}O_2$ catalysts, and $Au^{\delta+}$ species (Au^+ and Au^{3+}) are considered to be the more active species than Au^0 for oxidation reaction [51]. It is deduced that the appearance of $Au^{\delta+}$ may lead to the increasing the amount of surface active oxygen species (O_2^-, O^-) due to the decrease in the d-electron density of the Au atoms and the onset of reactivity to oxygen in air [52], and also results in the strong interaction between gold and supports. As shown in Fig. 10B, the O1s binding energies are located at 528.8, 530.7 and 532.0 eV, which are assigned to lattice oxygen species (O^{2-}) and chemisorption's oxygen species (O^- and O_2^-), respectively. The content ratio of $O_2^{\delta-}$ in catalysts remarkably increases after the introduction Au on $Ce_{0.8}Zr_{0.2}O_2$ support as shown in Table 4, which may be attributed to the effect of strong metal–oxide interaction to active oxygen species. Thus, the increasing of surfaces active oxygen species (O_2^-, O^-) would gives rise to unusual catalytic properties for deep oxidation reaction.

Fig. 10C shows the XPS spectra in the Ce 3d region. The four main $3d_{5/2}$ features at 881.7, 884.6, 888.1 and 897.7 eV corresponding to V, V′, V″ and V‴ components, while the $3d_{3/2}$ features at 900.3, 902.7, 907.3 and 916.1 eV corresponding to U, U′, U″ and U‴ components, respectively [53]. The signals V′ and U′, characteristics of Ce^{3+}, exist evidently in the 3DOM $Au/Ce_{0.8}Zr_{0.2}O_2$ catalyst in comparison with those of 3DOM $Ce_{0.8}Zr_{0.2}O_2$ catalyst [54]. The value of R^b (the Ce species ratio of Ce^{3+}/Ce^{4+}) increases from 0.252 ($Ce_{0.8}Zr_{0.2}O_2$) to 0.433 ($Au/Ce_{0.8}Zr_{0.2}O_2$) in Table 4. The increasing of Ce^{3+} content is contributed to the interaction between cerium and the surrounding atoms, which leads to an increase in the oxygen vacancies. It can be deduced that the interaction between cerium and gold may lead to a transference of the lattice oxygen in ceria over the surface of Au nanoparticles and maintaining cerium at the low-valent state. Thus, the gold atoms at the perimeter of the gold nanoparticles with the cerium or the ultrasmall Au clusters located near an oxygen vacancy bear a positive charge due to that Au atoms can be oxidized by the surface Ce atoms [55]. Combined with the XPS result of Zr 3d in Fig. 6D, the spectrum corresponding to level 3d of zirconium of 3DOM $Au/Ce_{0.8}Zr_{0.2}O_2$ catalyst has no change comparing with 3DOM $Ce_{0.8}Zr_{0.2}O_2$ catalyst. Therefore, we can deduce that Au atoms prefer to interact with cerium atoms in comparison with zirconium atoms, and the synergetic effect between gold and cerium leads to increasing the amounts of Ce^{3+} and $Au^{\delta+}$ in the 3DOM $Au/Ce_{0.8}Zr_{0.2}O_2$ catalyst. It indicates that there is a strong interaction between $Ce_{1-x}Zr_xO_2$ and gold due to the electron transformed from Au metal to Ce^{4+} in supports, and the amount of active oxygen species also increases due to the oxygen transference from ceria to Au. A strong metal–support interaction between Au atom and Ce atom is also observed by Raman spectra in Fig. 7, and the strong interaction is beneficial to the creation of the oxygen vacancies [41]. This is similar to the reported results on the strong Pt-ceria interaction by Vayssilov et al. [32]. In summary, the chemical or structural ordering may be responsible for the catalytic activity of $Au/Ce_{0.8}Zr_{0.2}O_2$ catalyst, which increases the amount of active oxygen species (O_2^-, O^-). This result is in good agreement with those of O_2–TPD and H_2–TPR measurements.

3.1.10. The results of NO oxidation

Fig. 11 shows the concentration change of NO_2 during NO oxidation over 3DOM $Au/Ce_{0.8}Zr_{0.2}O_2$ catalyst by the means of MS measurement. For comparison, the NO_2 concentration profiles of NO oxidation over 3DOM $Ce_{0.8}Zr_{0.2}O_2$ catalyst and the case without catalyst are also included. Almost no NO_2 was detected in the case without catalyst when the temperature was less than 500 °C, as shown in plot (a). However, when 3DOM $Ce_{0.8}Zr_{0.2}O_2$ catalyst was present, the NO_2 concentration remarkably increased, and it was the largest on a typical catalyst of 3DOM $Au/Ce_{0.8}Zr_{0.2}O_2$ catalyst, as shown in plot (b) and (c). The NO_2 concentration over 3DOM $Au/Ce_{0.8}Zr_{0.2}O_2$ catalyst increases dramatically when the temperature is higher than 260 °C. The peak temperature of NO_2 concentration profile over 3DOM $Au/Ce_{0.8}Zr_{0.2}O_2$ catalyst shifted to the lower temperature by about 50 °C in comparison with that

Table 3
The analysis results of surface active oxygen species on the different catalysts by O_2–TPD measurements.

Sample (3DOM)	α (O_2^-)		β (O^-)		γ (O^{2-})	
	T (°C)	S_α[a] (10^7)	T (°C)	S_β[a] (10^7)	T (°C)	S_γ[a] (107)
Au/CeO_2	190	2.03	408	13.35	703	23.25
$Au/Ce_{0.8}Zr_{0.2}O_2$	188	2.10	420	13.25	664	22.10
$Au/Ce_{0.7}Zr_{0.3}O_2$	187	1.76	430	11.53	665	20.86
$Au/Ce_{0.5}Zr_{0.5}O_2$	188	1.73	443	8.56	667	15.28
Au/ZrO_2	188	1.51	459	3.08	–	–

[a] Determined by the peak area of surface oxygen species in O_2–TPD profile.

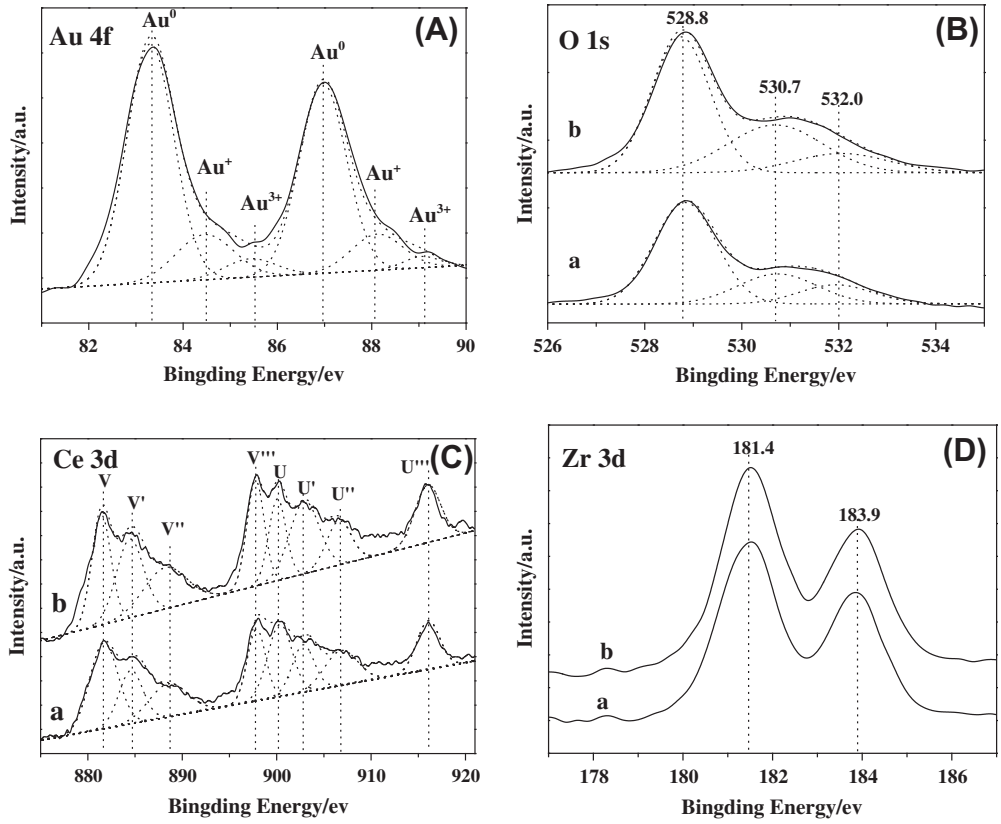

Fig. 10. X-ray photoelectron spectra (XPS) of Au 4f (A), O 1s (B), Ce 3d (C) and Zr 3d (D) regions for the 3DOM $Ce_{0.8}Zr_{0.2}O_2$ (a) and Au/$Ce_{0.8}Zr_{0.2}O_2$ (b) catalysts.

Table 4
Surface composition and oxidation state of Au, Ce and O species dervied from XPS analyses.

Sample (3DOM)	Au species				Ce species				O species		
	Au^0	Au^+	Au^{3+}	R[a]	Ce^{3+}	Ce^{4+}	R[b]	O_2^-	O_2^{2-}	O^{2-}	R[c]
$Ce_{0.8}Zr_{0.2}O_2$	–	–	–	–	20.1	79.9	0.252	13.7	23.1	63.2	0.582
Au/$Ce_{0.8}Zr_{0.2}O_2$	69.3	20.7	10.0	0.443	30.2	69.8	0.433	14.2	34.1	51.7	0.934

[a] Determined by the Au species ratio of the $Au^{\delta+}(Au^+ + Au^{3+})/Au^0$.
[b] Determined by the Ce species ratio of the Ce^{3+}/Ce^{4+}.
[c] Determined by the oxygen species ratio of the adsorbed oxygen ($O_2^- + O_2^{2-}$)/lattice oxygen (O^{2-}).

of 3DOM $Ce_{0.8}Zr_{0.2}O_2$ catalyst, which is accorded with that of CO_2 concentration profile over the catalyst at high temperature in TPO process. It partially explains the high catalytic activity of 3DOM Au/$Ce_{0.8}Zr_{0.2}O_2$ catalyst for soot combustion at relatively high temperature (>250 °C).

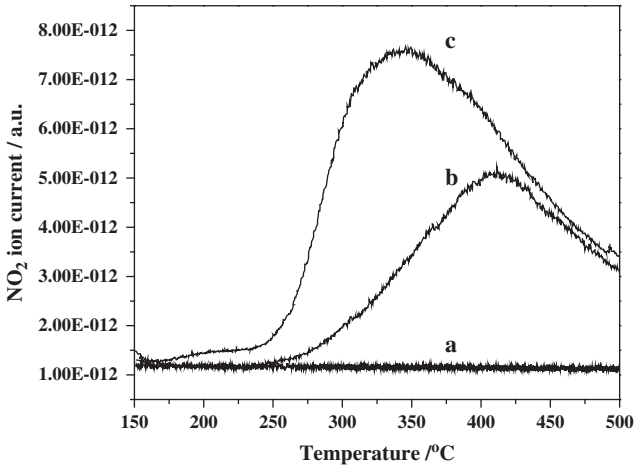

Fig. 11. The outlet NO_2 ion current curves during NO oxidation process. (a) without catalyst; (b) 3DOM $Ce_{0.8}Zr_{0.2}O_2$ catalyst; (c) 3DOM Au/$Ce_{0.8}Zr_{0.2}O_2$ catalyst.

3.2. Reactions

3.2.1. TPO reactions

The TPO experimental results of diesel soot oxidation over the particle $Ce_{1-x}Zr_xO_2$, 3DOM $Ce_{1-x}Zr_xO_2$ solid solutions and Au/$Ce_{1-x}Zr_xO_2$ catalysts are listed in Table 5. For comparison, the TPO result of bare soot (i.e., without catalyst) is also included, and its T_{10}, T_{50}, T_{90} and S^m_{CO2} are 482, 585, 646 °C and 55.0%, respectively. The TPO results show that all the catalysts can promote soot oxidation, and the 3DOM $Ce_{1-x}Zr_xO_2$ catalysts have higher catalytic activity than those of particle catalysts, which are attributed to the open and interconnected macropores structure giving more contact area between soot and catalyst under the condition of soot embedded into the inner pores with the help of airflow. The catalytic activity for soot oxidation is remarkably enhanced after Au nanoparticles supported on the surface of 3DOM $Ce_{1-x}Zr_xO_2$ solid solutions, especially T_{10} and S_{CO2}. Among the different ratios of Ce/Zr in 3DOM Au/$Ce_{1-x}Zr_xO_2$ catalysts, Au/$Ce_{0.8}Zr_{0.2}O_2$ catalyst exhibits the best ignition catalytic performance under loost contact condition, which might be assigned to the fact of the synergetic effect of the interface between Au nanoparticle and $Ce_{0.8}Zr_{0.2}O_2$ carrier to dioxygen activation. However, there is a negative effect on the activity (T_{10}) for soot combustion with the increasing of Zr

Table 5
The temperatures and the selectivity to CO_2 for soot combustion over without catalyst, the particle $Ce_{1-x}Zr_xO_2$, 3DOM $Ce_{1-x}Zr_xO_2$ solid solutions and $Au/Ce_{1-x}Zr_xO_2$ catalysts (loose contact).

Catalysts	T_{10}			T_{50}			T_{90}			S^m_{CO2} (%)		
	Particles	3DOM	Au/3DOM	Particles	3DOM	Au/3DOM	Particles	3DOM	Au/3DOM	Particles	3DOM	Au/3DOM
CeO_2	370	337	247	445	390	349	479	432	396	98.0	97.3	99.8
$Ce_{0.9}Zr_{0.1}O_2$	364	329	240	442	378	361	487	420	407	98.3	85.7	99.7
$Ce_{0.8}Zr_{0.2}O_2$	381	328	232	449	394	365	491	432	418	97.1	88.4	99.8
$Ce_{0.7}Zr_{0.3}O_2$	382	328	248	451	403	375	493	446	419	96.5	84.8	99.8
$Ce_{0.6}Zr_{0.4}O_2$	384	352	263	461	415	377	505	457	423	95.2	82.6	99.7
$Ce_{0.5}Zr_{0.5}O_2$	390	357	299	465	416	383	515	458	426	92.3	80.1	99.5
$Ce_{0.3}Zr_{0.7}O_2$	398	355	322	475	422	407	520	467	452	84.1	78.7	98.5
ZrO_2	470	367	353	580	485	430	639	543	477	60.2	76.9	97.8
Soot	482			585			646			55.0		

Reaction conditions: reaction gas, 5% O_2 and 0.2% NO in Ar, 50 ml min^{-1}; the soot/catalyst mass ration is 1/10.

content above 20%. In addition, the regular catalytic activity (T_{50} and T_{90}) of 3DOM $Au/Ce_{1-x}Zr_xO_2$ catalysts is different from the result of T_{10}. The 3DOM Au/CeO_2 catalyst exhibits the best catalytic performance for soot combustion at higher temperature, which T_{50} and T_{90} are 349 and 396 °C, respectively. It indicates that there is a negative effect on the activity (T_{50} and T_{90}) of 3DOM $Au/Ce_{1-x}Zr_xO_2$ catalysts with the increasing of Zr content. The TPO results of 3DOM Au/CeO_2 and $Au/Ce_{0.8}Zr_{0.2}O_2$ catalysts on three cycles are shown in Table S3. The catalytic performance of the catalyst remarkably becomes worse after one cycle due to the low thermal stability of supported Au catalysts [28]. Thus, it is an important issue to prevent the sintering of Au nanoparticles and it is worth investigating in the further work.

To more clearly investigate the process of soot combustion, the CO_2 concentrations (C_{CO2}) as a function of reaction temperature are shown in Fig. S7. The TPO patterns of soot combustion on the 3DOM $Au/Ce_{1-x}Zr_xO_2$ catalysts exhibit two peaks of temperature centered at ~235 °C and ~360 °C. The peak of the CO_2 concentration profiles for soot combustion over the 3DOM $Au/Ce_{1-x}Zr_xO_2$ catalysts shifted to the lower temperature comparing with those over the 3DOM $Ce_{1-x}Zr_xO_2$ catalysts. And with increasing of the content of Zr-doped in catalysts, the CO_2 concentration peak at 235 °C decreased, and the position of the CO_2 concentration peak (~360 °C) shifted to the higher temperature. It is suggested that the catalytic performances of supported Au catalysts are strongly dependent on the nature of supports. And the catalytic mechanism of 3DOM $Au/Ce_{1-x}Zr_xO_2$ catalysts at high temperature (>260 °C) is different from that of the low temperature (<260 °C).

The S^m_{CO2} in the soot oxidation over 3DOM $Ce_{1-x}Zr_xO_2$ catalysts are markedly decreased in contrast to particle-type catalysts in Table 5. It is attributed to the open and interconnected macropores giving less choice for the contact between CO and catalyst, and the CO passed through the 3DOM catalysts faster than soot. To more clearly observe the selectivity of CO_2 in the process of soot combustion, the S_{CO2} profiles of soot oxidation over the 3DOM $Ce_{1-x}Zr_xO_2$ and $Au/Ce_{1-x}Zr_xO_2$ catalysts are shown in Fig. S8. The CO_2 selectivities over the 3DOM $Ce_{1-x}Zr_xO_2$ catalysts were always less than 90% except for CeO_2, and the higher value of S_{CO2} over 3DOM $Ce_{1-x}Zr_xO_2$ catalysts are in narrow temperature range (300 °C~450 °C). However, the S_{CO2} is largely enhanced after Au nanoparticles supported on the surface of 3DOM $Ce_{1-x}Zr_xO_2$ solid solutions in Fig. S8B, and it is nearly 100% in wider temperature range (200–450 °C), which can ensure that the CO emitted from cars is immediately removed under the practical temperature of diesel engine emissions (150–400 °C). And the S_{CO2} over the 3DOM $Au/Ce_{1-x}Zr_xO_2$ catalysts is influenced by the supports with the different ratios of Ce/Zr.

3.2.2. Isothermal reactions

The intrinsic activity of catalyst is based on turnover frequency (TOF), which is defined as the ratio of reaction rate to the active site density of catalysts. The reaction rate of soot combustion is determined by an isothermal reaction at 210 and 300 °C in the kinetic regime, and the uniform macroporous structure of catalysts could exclude the intraparticle mass transport limitations. The reaction rate for soot combustion (the concentration of CO_2 per unit time) was calculated according to the slope of the lines, as shown in Fig. S9. The reaction rate for soot combustion over 3DOM $Ce_{1-x}Zr_xO_2$ catalysts at 210 and 300 °C can be negligible in contrast to that of 3DOM $Au/Ce_{1-x}Zr_xO_2$ catalysts, for example, the R_{210} over 3DOM $Ce_{0.8}Zr_{0.2}O_2$ catalyst is only 0.022×10^{-6} mol min^{-1} and the R_{300} over 3DOM CeO_2 catalyst is only 0.091×10^{-6} mol min^{-1}. Table 6 lists the quantified values of the reaction rate, the total loading amount of Au, and the TOF for soot combustion over the 3DOM $Au/Ce_{1-x}Zr_xO_2$ catalysts under the same condition as that of TPO reaction. The TOF values of the catalysts are quite large, indicating that the Au sites are very active for the soot combustion. The TOF value of 3DOM $Au/Ce_{0.8}Zr_{0.2}O_2$ catalyst (1.31×10^{-3} S^{-1}) was six times as that of 3DOM Au/ZrO_2 catalyst (0.21×10^{-3} S^{-1}) at 210 °C, and the TOF value of 3DOM Au/CeO_2 catalyst (2.70×10^{-3} S^{-1}) was approximately 2.5 times as that of 3DOM Au/ZrO_2 catalyst (1.12×10^{-3} S^{-1}) at 300 °C, despite a very similar size distribution of Au nanoparticles being observed by TEM images. Indeed, as the reaction of soot oxidation occurs at same temperature and the total numbers of exposed surface atoms of Au nanoparticle with similar size distribution are almost identical, other factors such as the nature of the supports and activated surface oxygen species may be involved. The oxygen storage ability of Ce-based supports is well-known and this, allied to the ease with which the surface oxygen can be reduced, may influence upon the reaction, in contrast to the non-reducible ZrO_2 supports. Among all the tested catalysts, the TOF values of 3DOM $Au/Ce_{0.8}Zr_{0.2}O_2$ catalyst is largest at 210 °C, while that of 3DOM Au/CeO_2 catalyst is largest at 300 °C, indicating that there are different catalytic mechanisms for soot oxidation in the different reaction temperature region.

4. Discussion

4.1. The effect of the supports on catalytic performance for soot combustion

It is reported that the nature of the support material can influence the catalytic activity of the resulting gold catalysts [56]. The effects of supports on catalytic performance for soot combustion are mainly from two aspects: structure and redox property. The reaction for catalytic combustion of soot is a typical heterogeneous catalytical reaction, which takes place at the three-phase boundary among a solid catalyst, a solid reactant (soot) and gaseous reactants (O_2, NO). The efficiency of catalyst for solid–solid reaction is strongly influenced by the contact between soot and catalyst. In many studies, the outer surface of general catalysts is only available for soot combustion because their pore diameters (usually

Table 6
The total loading amount of Au, reaction rate and TOF values for soot combustion over the 3DOM $Au/Ce_{1-x}Zr_xO_2$ catalysts at 210 and 300 °C.

Catalysts (3DOM)	Au actual content/wt.% [a]	Au/mol × 10^{-6}	210 °C		300 °C	
			R (mol min^{-1})×10^{-6}	TOF_{Au} (S^{-1} × 10^{-3})	R (mol min^{-1})×10^{-6}	TOF_{Au} (S^{-1} × 10^{-3})
Au/CeO_2	1.3	6.6	0.48	1.20	1.07	2.70
$Au/Ce_{0.9}Zr_{0.1}O_2$	1.3	6.6	0.51	1.29	0.92	2.34
$Au/Ce_{0.8}Zr_{0.2}O_2$	1.5	7.6	0.60	1.31	0.89	1.95
$Au/Ce_{0.7}Zr_{0.3}O_2$	1.4	7.1	0.48	1.12	0.82	1.92
$Au/Ce_{0.6}Zr_{0.4}O_2$	1.3	6.6	0.39	0.97	0.74	1.87
$Au/Ce_{0.5}Zr_{0.5}O_2$	1.2	6.1	0.28	0.77	0.59	1.62
$Au/Ce_{0.3}Zr_{0.7}O_2$	1.3	6.6	0.16	0.39	0.54	1.37
Au/ZrO_2	1.2	6.1	0.08	0.21	0.41	1.12

Reaction conditions: reaction gas, 5% O_2 and 0.2% NO in Ar, 50 ml min^{-1}; the soot/catalyst mass ratio is 1/10.
[a] Determined by inductive coupled plasma atomic emission spectrometry.

<10 nm or even non-porous) are much smaller than the particle diameter of soot (~25 nm) observed by the TEM image in Fig. S4. Therefore, to meet the needs to increase contact area, 3DOM materials with uniform pore size (>50 nm) and periodic voids interconnected through open windows are designed and synthesized by colloidal crystal templates method. 3DOM $Ce_{1-x}Zr_xO_2$ catalysts have higher catalytic activities than the corresponding particle catalysts. The pathway of reaction for soot combustion can be summarized: the soot particles can easily enter the interior of 3DOM catalysts and have less resistance going through the catalyst with the help of the airflow in the reaction under loose contact between soot and catalysts. The direct evidence is observed by TEM images of the composition of 3DOM catalyst and soot with the same condition of TPO reaction until 250 °C in Fig. 12. It is shown that 3DOM structure still kept intact in the reaction process, and soot particles entered the inner pores of 3DOM $Au/Ce_{0.8}Zr_{0.2}O_2$ catalyst with the help of the airflow. The voids of 3DOM $Au/Ce_{0.8}Zr_{0.2}O_2$ catalyst are filled with soot particles in the Fig. 12B and C, indicating that 3DOM structure is a desirable feature for diesel soot combustion. The perfect macroporous structure provides the ideal reaction space for solid reactants (diesel soot). The number of contact points between soot and catalysts should be increased dramatically. However, the result also shows that 3DOM structure is adverse to improving the selectivity of CO_2 as shown in Table 5. The production of relatively large amounts of CO during soot combustion is because that the small molecule of CO is fast to pass through the 3DOM catalysts with the big pore size which is disadvantageous to the contact between CO and catalyst. But 3DOM $Au/Ce_{1-x}Zr_xO_2$ bifunctional catalysts exhibited much higher S_{CO2} for soot oxidation, which is easy for understanding. The supported Au catalysts exhibit a surprisingly high activity for low-temperature CO oxidation [11].

The catalytic activities of different materials with the same 3DOM structure and Au particle size for soot combustion are obvious different as shown in Table 5, indicating that the intrinsic catalytic properties are strongly related to support themselves. The reaction of soot combustion is a kind of deep oxidation reaction. The catalysis nature of the reaction is the redox process. Therefore, the intrinsic catalytic performances of catalysts are related to the redox property determined by the nature of supports. As shown in Fig. 8A, 3DOM $Ce_{0.8}Zr_{0.2}O_2$ support showed better redox property at low temperature (350 °C). It can be deduced that the mobility of lattice oxygen increases from the bulk to the surface with the moderate Zr-doped content into the ceria lattice. It leads to the change of the lattice and the increase in the channel diameter for lattice oxygen migration, since the ion radius of Zr^{4+} (0.086 nm) is smaller than that of Ce^{4+} (0.101 nm) [57]. The effectiveness of the catalysts are related to their ability to deliver oxygen from the lattice to the surface of soot in a wide temperature region, and cerium-rich samples have a stronger ability to donate oxygen for soot oxidation, i.e., the cerium-rich samples have high mobility of lattice oxygen, which are consistent with the results of O_2–TPD measurements. For example, in the O_2–TPD profile of 3DOM $Ce_{1-x}Zr_xO_2$ catalysts, the mobility of oxygen species over $Ce_{0.8}Zr_{0.2}O_2$ sample is the highest, and the mobility of oxygen species will be influenced by the Zr-doped content. The generation of "active oxgen species" induced by Zr cations would explain the high activity of 3DOM $Au/Ce_{0.8}Zr_{0.2}O_2$ catalyst for soot combustion at low temperature. Compared with the catalytic activities of 3DOM $Ce_{1-x}Zr_xO_2$ and $Au/Ce_{1-x}Zr_xO_2$ catalysts, it could be concluded that the better redox property of supports (different Ce/Zr ratios) can improve the catalytic activity for soot combustion, especially at the low temperatures.

4.2. The effect of the Au nanoparticle on catalytic performance for soot combustion

The catalytic activities for soot oxidation are remarkably enhanced after the introduction of Au nanoparticles on the surface of 3DOM $Ce_{1-x}Zr_xO_2$ solid solutions, especially T_{10} and S_{CO2}. As far as the role of supported Au nanoparticle in oxidation reaction is concerned, it has not been well recognized whether the reaction proceeds exclusively on metallic gold particles or it might occur preferentially at the edges of gold particle involving either sites on the adjacent support or on gold atoms influenced by the support. Generally speaking, the catalytic performances of gold catalysts strongly depend on the particle size since Au nanoparticles can activate molecule oxygen. It is not the first time that the role of oxygen is evoked particularly in oxidation reactions over gold nanoparticles [52]. Small gold particles lose its metallic character due to an increase of the d-electron density and also to a high degree of surface de-saturation, which leads to a higher reactivity. Our previous work [28] showed that the catalytic performance for soot combustion was strongly depended on the size of supported Au nanoparticles, and the catalytic activity was correlated with the active oxygen species on Au. In this study, the average sizes of supported Au particles are equivalent, but the catalytic activities for soot combustion over different supports are obviously different, indicating that besides the particle size, the other factors should also govern the catalytic performances of the catalysts. The properties of supports would play an important role in catalyzing soot oxidation. The analysis results in Fig. 13 showed that the T_{10} and T_{50} values are closely correlated with the amount of surface active oxygen species (α) and (β) which are varying from the Ce/Zr ratios in catalysts. Based on the experimental observations by H_2–TPR, O_2–TPD and XPS measurements, we can deduce that the active oxygen species over 3DOM $Au/Ce_{1-x}Zr_xO_2$ catalysts may be derived from the two approaches (or "generator"): one is direct activation of oxygen on the surface of gold nanoparticles. The other is derived from the synergetic effect of metal (Au)-support (Ce)

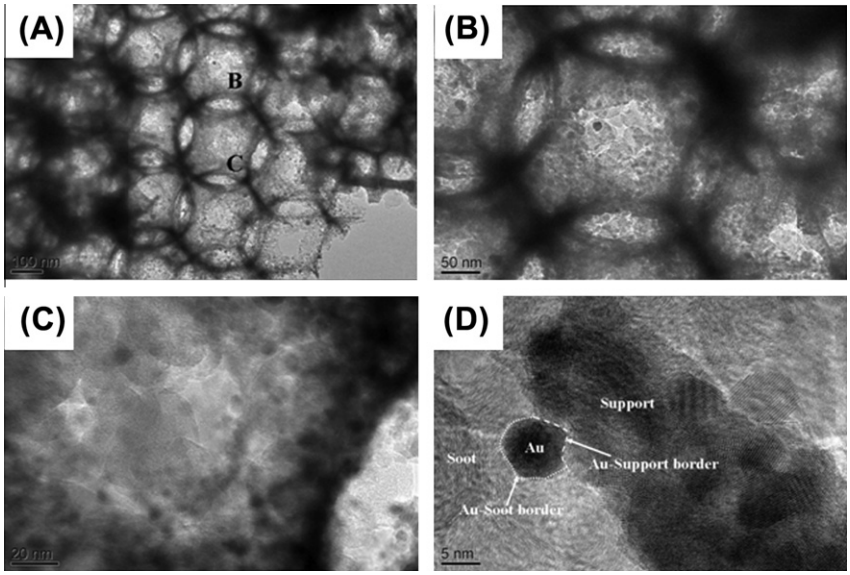

Fig. 12. TEM (A–C) and HRTEM images (D) of 3DOM $Au/Ce_{0.8}Zr_{0.2}O_2$ catalyst after undergone the TPO reaction until 250 °C. Reaction conditions: reaction gas, 5% O_2 and 0.2% NO in Ar, 50 ml min; the soot/catalyst mass ratio is 1/10.

which the induced support may give rise to the fact that Ce-based supports serve as a reservoir for oxygen in the oxidation reaction. The interaction between support and gold may lead to a transfer of the lattice oxygen in support or the adsorption of oxygen from the support vacancies at the low temperatures, though this effect is usually observed above 300 °C for pure supports [58]. The active oxygen species derived from the metal–support interaction is more important for soot combustion than the first one. Therefore, 3DOM $Au/Ce_{1-x}Zr_xO_2$ catalysts ($x \leqslant 0.2$) have good catalytic performance for soot combustion due to a strong ability to donate oxygen of cerium-rich samples. For instance, the TOF value of 3DOM $Au/Ce_{0.8}Zr_{0.2}O_2$ catalyst is six times as that of 3DOM Au/ZrO_2 catalyst at 210 °C. However, the active oxygen species predominating in the oxidation reaction general stays at the surface of 3DOM $Au/Ce_{1-x}Zr_xO_2$ catalysts. Thus, the question is how the active oxygen species migrate from the surface of catalyst to soot and what will form?

It can be found in the fact that the contact area for solid–solid reactions, i.e., between catalytic sites and the soot, is of great importance. Since the number of contact points is proportional to the catalyst concentration, one can expect an increase in activity with higher surface loadings. In many studies, the catalytic performances for soot combustion are very excellent under tight conditions between soot and catalyst because of their good contact. However, it is loose contacts between catalysts on the surface of filter and soot particles under practical conditions. Thus, it is significantly important to study and design the active catalysts for improving the contact capacity for soot combustion under loose contact conditions. In our previous works [59], the high activities have been related to the low melting points of active site, which ensure a good contact between soot and catalyst. The catalytic mechanism for soot oxidation has been reported that there is a correlation between melting temperature of catalyst and its catalytic activity [60]. As shown in Fig. 12D, Au nanoparticles supported on the inner surface of 3DOM structure catalysts are able to further increase the contact between soot and catalyst because of the "wetting" and surface mobility capability of Au nanoparticles with low melting points [61]. The contact between soot and Au nanoparticles is a tight-like contact type in the solid–solid reactions, in which supported Au nanoparticle is the media center for tight-like contact between

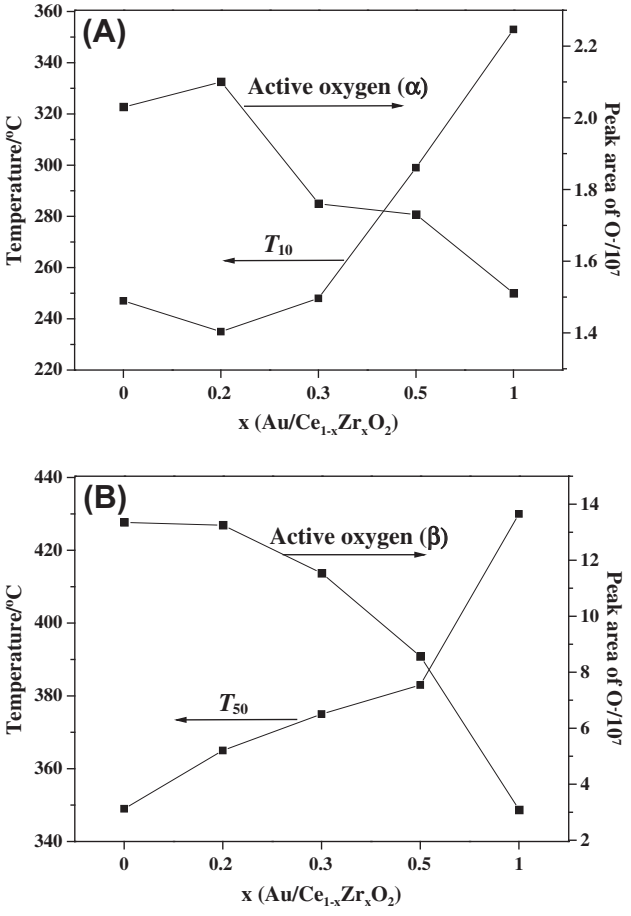

Fig. 13. The relation between the peak area of surface active oxygen species by O_2–TPD and the soot combustion temperature over 3DOM $Au/Ce_{1-x}Zr_xO_2$ catalysts with different values of x. T_{10} and the active oxygen specie (α) (A) and T_{50} and the active oxygen specie (β) (B) as a function of x.

$Ce_{0.8}Zr_{0.2}O_2$ support and soot particles, indicating that the catalytic performance for soot combustion would be enhanced because the active oxygen species could migrate from the catalyst to the soot

particle by the way of spillover. Therefore, 3DOM Au/$Ce_{1-x}Zr_xO_2$ catalysts exhibited super catalytic performance (T_{10}) for soot combustion at the low temperatures.

4.3. The effect of NO on the catalytic performance

In the famous CRT technology, NO_x is acting as an efficient mobile oxidizing agent, which accesses the soot combustion and causes light-off of soot in an appropriate temperature range, since the oxidizing ability of NO_2 is stronger than that of O_2. However, most of NO_x in diesel exhaust gas is NO, NO_2 is almost non-existent. In the CRT system, the removal of soot particles by oxidation with NO_2 is achieved by placing an oxidation catalyst upstream of the trap in order to convert NO in the exhaust into NO_2 [2,62]. This mechanism subtly changed solid (soot)–solid (catalyst) contact into solid (soot)–gas (NO_2)–solid (catalyst) contact. A similar mechanism is found for soot combustion over 3DOM $Ce_{1-x}Zr_xO_2$-supported Au nanoparticle catalysts. As shown in Fig. S10, the profiles of CO_2 concentration over the typical catalysts show a similar variation trends under the condition of the presence or absence of NO. In the low temperatures range (<250 °C), the C_{CO2} profiles are very similar to the cases with or without NO. It suggested that the catalytic activity at the low temperatures is not mainly correlated with the NO gas as oxidizing agent. But at relatively high temperature (>250 °C), the C_{CO2} peak in the presence of NO is higher and narrower than the case without NO, indicating that the catalytic performances of supported Au catalysts are strongly related to the NO gas. It is attributed to that 3DOM Au/$Ce_{1-x}Zr_xO_2$ catalysts can promote NO oxidizing to NO_2 which is used as intermediate to catalyze soot oxidation. The strong oxidation ability of the catalyst for NO oxidation is consistent with the results of in situ DRIFT measurement in Fig. S11. The identification of the adsorbed species proves that NO_x is stored in the forms of nitrite/nitrates on the catalyst surface, for which NO must be partially oxidized to NO_2 in a preceding step. This also explains that NO_2 can be released from the surface of catalyst at higher temperatures (>250 °C).

The direct evidence of NO_2 produced is detected by the means of in situ MS measurement. As shown in Fig. 11, bare soot exhibited no activity for NO_2 production, and the NO_2 level reached with bare soot is the same as that measured in the initial time of the reaction. In comparison, 3DOM $Ce_{0.8}Zr_{0.2}O_2$ oxide was quite effective for NO oxidation to NO_2 when reaction temperature greater than 250 °C. The NO_2 concentration obtained over this catalyst increased with temperature rising until the thermodynamic equilibrium of the equation ($NO + 1/2O_2 \leftrightarrow NO_2$) was fulfilled and then it decreased at higher temperatures following thermodynamics profile. The peak temperature for the production of NO_2 on 3DOM Au/$Ce_{0.8}Zr_{0.2}O_2$ catalyst is about 350 °C, which is much lower than that of 3DOM $Ce_{0.8}Zr_{0.2}O_2$ oxide. The NO_2 concentration over the 3DOM Au/$Ce_{0.8}Zr_{0.2}O_2$ catalyst is greater than that of the bare 3DOM $Ce_{0.8}Zr_{0.2}O_2$ oxide, resulting in a major contribution of the produced NO_2 to the soot oxidation process. The strong oxidizing ability of 3DOM Au/$Ce_{0.8}Zr_{0.2}O_2$ catalyst for NO oxidation is consistent with the results of H_2–TPR. Thus, 3DOM Au/$Ce_{0.8}Zr_{0.2}O_2$ catalyst should give much higher catalytic activity for soot combustion. In summary, according to the results of the effect of NO oxidation experiment, in situ DRIFT and in situ MS detection, it was found that NO is oxidized to NO_2 over the catalyst. Then, NO_2 acts as the oxidizing agent for soot combustion. The NO_2 concentration over the 3DOM Au/$Ce_{0.8}Zr_{0.2}O_2$ catalyst is higher than that of the bare 3DOM $Ce_{0.8}Zr_{0.2}O_2$ oxide. This can partially explain the strong synergistic effect of gold and cerium in catalyst on the soot oxidation.

4.4. Mechanism consideration

Based on the above results and discussions, the following three reasons can explain the high catalytic activities of 3DOM $Ce_{1-x}Zr_xO_2$-supported Au nanoparticle catalysts for soot combustion. First of all, the redox property of catalyst determines its intrinsic activity. The nanocomposite structure bifunctional materials, both nanometric crystal of $Ce_{1-x}Zr_xO_2$ supports and Au nanoparticles active component, possess the strong redox ability. It is attributed to that supported Au nanoparticles have the super capability of the adsorption and activation of oxygen in air, and there is a synergistic effect to donate the active oxygen species because the interaction between cerium and gold may lead to transference of the lattice oxygen in support and increase the amount of oxygen vacancies. Therefore, the intrinsic activity of 3DOM Au/$Ce_{1-x}Zr_xO_2$ catalysts is very excellent. Secondly, the good contact between catalyst and soot is a necessary external condition. It is significantly important for the migration of active oxygen species from catalyst to soot particle in the typical reaction of heterogeneous catalysis. 3DOM structure is a desirable feature for diesel soot combustion. The soot particles can be diffused into the inner pores of 3DOM catalysts with the help of airflow in the reaction under loose contact condition between soot and catalysts. Thus, the surface area of inner pores is to reach the maximum application. And the supported Au nanoparticle could further improve the contact between catalyst and soot particle with the tight-like contact. The good contact is a necessary condition for the migration of active oxygen species from catalyst to soot particle which is a crucial factor affecting the catalytic performance for soot combustion. Thirdly, similarly to noble metal Pt catalysts, 3DOM Au/$Ce_{1-x}Zr_xO_2$ catalysts can efficiently catalyze NO to NO_2. The NO_2 can directly oxidize the soot particle to CO_2, which ensure the good indirect contact performances between catalysts and soot particles. In addition, supported Au catalysts exhibit the high selectivity to CO_2 production in soot combustion reaction which avoid secondary pollution and suppress emission of CO. Therefore, 3DOM Au/$Ce_{1-x}Zr_xO_2$ catalysts are the good catalyst system for soot combustion under loose contact conditions.

All the results above allow us to propose a mechanism for soot combustion with NO and O_2 over 3DOM Au/$Ce_{1-x}Zr_xO_2$ catalysts at the different temperatures. The pathway of reaction for soot combustion can be summarized and shown in Scheme 1. First of all, active oxygen species over the surface of Au nanoparticle derived from two approaches of which one is direct activation of oxygen by Au nanoparticle (1) and the other is derived from the induced support with the interaction between Au atom and Ce atom (2)–(3). The active oxygen species would migrate from catalyst to the carbon surface by the contact site between soot and catalyst. At low temperatures (<240 °C) in Scheme 1A, Au nanoparticle can contact with catalyst and soot particle, and active oxygen species can spill over to the free carbon sites on soot to give off CO or CO_2 (4) [63]. Therefore, the catalytic performance of supported Au catalyst is dependent on the ability to donate oxygen of supports (Ce/Zr ratio). The TOF value of 3DOM Au/$Ce_{0.8}Zr_{0.2}O_2$ catalyst is six times as much as the value of 3DOM Au/ZrO_2 catalyst at 210 °C since $Ce_{0.8}Zr_{0.2}O_2$ support exhibit the stronger capability to activate oxygen than that of ZrO_2. With the increasing of the reaction temperature (240∼260 °C) in Scheme 1B, the amount of active oxygen species (O^-) over Au nanoparticles decreases because the rate of oxygen desorption increases confirmed by O_2–TPD results, and the part of active oxygen species are consumed by the oxidation of NO–NO_2. There is no adequate active oxygen species (O^-) to migrate to the surface of soot particle. Thus, the rate of catalytic soot combustion decreases. At the relatively high temperatures (>260 °C) in Scheme 1C, the large amount of NO can be oxidized to NO_2 over the catalyst (5). And NO_2 can directly react with the free carbon sites to give off CO or CO_2 (6). Therefore, the

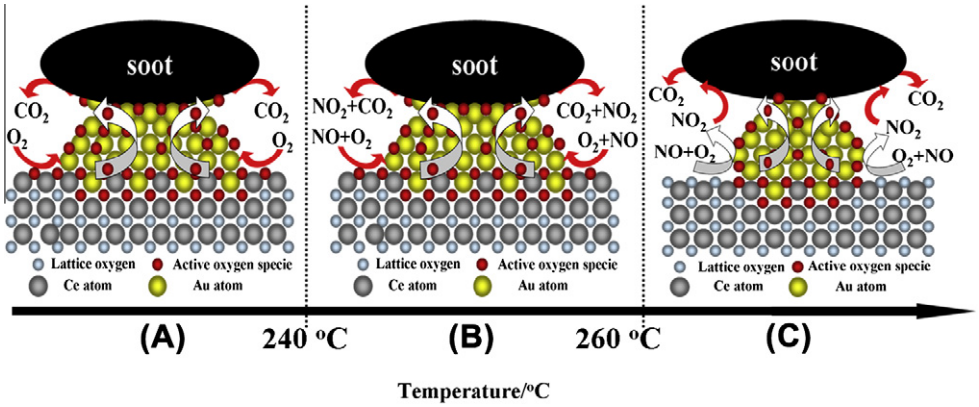

Scheme 1. Mechanism illustration of soot combustion over 3DOM Au/$Ce_{1-x}Zr_xO_2$ catalysts at different temperature in the presence of O_2 and NO.

rate of soot combustion at relatively high temperatures remarkably increases owing to the combined effect of the active oxygen species (O^-, O^{2-}) and NO_2, especially NO_2 plays a dominant role in this process. In addition, in the whole process of catalytic soot combustion, the Au-based catalyst exhibits high catalytic activity for CO oxidation (7). In summary, the whole reaction process for soot combustion over the 3DOM Au/$Ce_{1-x}Zr_xO_2$ catalysts may be described as following equations:

$$O_2 + Au \rightarrow Au{-}O^* \quad (1)$$

$$Ce^{4+} + Au^0 \rightarrow Ce^{3+} + Au^+ + V_O \quad (2)$$

$$O_2 + V_O \rightarrow O^* \quad (3)$$

$$O^* + C{=}C \rightarrow CO \text{ or } CO_2 \quad (4)$$

$$NO + O^* \rightarrow NO_2 \quad (5)$$

$$NO_2 + C{=}C \rightarrow NO_x + CO \text{ or } CO_2 \quad (6)$$

$$CO + Au{-}O^* \rightarrow Au + CO_2 \quad (7)$$

O^* represents the surface activate oxygen species; V_O represents a surface oxygen vacancy; C=C represents the free carbon (soot particle). The catalytic activity of soot combustion on 3DOM Au/$Ce_{1-x}Zr_xO_2$ catalysts in NO + O_2 can be explained by the proposed mechanism. The synergic effect between Au particle and support play an essential role in the high catalytic activity for soot combustion.

5. Conclusions

We successfully fabricated 3DOM $Ce_{1-x}Zr_xO_2$-supported Au nanoparticle bifunctional catalysts by GBMR method. The macropores are highly ordered and interconnected one another by small pore windows. Gold nanoparticles with similar particle sizes are highly dispersed on the surface of the pore wall of different supports. 3DOM Au/$Ce_{1-x}Zr_xO_2$ catalysts exhibit the large total pore volume (~3.3 ml g^{-1}) and the porosity (~92%).

The nanocomposite structure materials, between nanometric crystal particle of 3DOM $Ce_{1-x}Zr_xO_2$ carriers and Au nanoparticle active components, possess the strong metal–support interaction. The metal (gold)-support (cerium) synergetic effect is favorable for the transference of the lattice oxygen in supports, and for increasing the amounts of oxygen vacancies and active oxygen species. 3DOM Au/$Ce_{1-x}Zr_xO_2$ catalysts exhibited good catalytic performances for soot oxidation, which is strongly related to the role of supports including the structure and the active oxygen supply pathways. The TPO and TOF results of 3DOM Au/$Ce_{1-x}Zr_xO_2$ catalysts for soot combustion are in accordance with the amount of active oxygen species (O_2^-, O^-).

The reaction pathway for soot combustion over 3DOM Au/$Ce_{1-x}Zr_xO_2$ catalysts can be divided into two sections. At the low reaction temperature, the soot particles are direct oxidized by active oxygen species migrated from the surface of supported Au catalysts. At the relatively high temperatures, the combined effects of the active oxygen species and NO_2 enhance the rate of soot combustion, especially NO_2 as an intermediate reactant plays a dominant role.

Acknowledgments

This work was supported by the National Natural Science Foundation of China (Nos. 20833011, 21177160, 21173270, and 20803093), the Program for New Century Excellent Talents in University of China (NCET-10-0811), the 863 program of China (No. 2009AA06Z313), CNPC Project (2011D-4604-0101), and Innovation Foundation (2010D-5006-0402).

Appendix A. Supplementary material

Supplementary data associated with this article can be found, in the online version, at doi:10.1016/j.jcat.2011.11.006.

References

[1] W.F. Shangguan, Y. Teraoka, S. Kagawa, Appl. Catal. B 16 (1998) 149.
[2] J. Oi-Uchisawa, S. Wang, T. Nanba, A. Ohi, A. Obuchi, Appl. Catal. B 44 (2003) 207.
[3] F.E. López-Suárez, A. Bueno-López, M.J. Illán-Gómez, Appl. Catal. B 84 (2008) 651.
[4] R. Kimura, J. Wakabayashi, S.P. Elangovan, M. Ogura, T. Okubo, J. Am. Chem. Soc. 130 (2008) 12844.
[5] J.L. Hueso, A. Caballero, M. Ocaña, A.R. González-Elipe, J. Catal. 257 (2008) 334.
[6] I. Atribak, A. Bueno-López, A. García-García, P. Navarro, D. Frías, M. Montes, Appl. Catal. B 93 (2010) 267.
[7] Y. Zhang, L. Zhang, J. Deng, H. Dai, H. He, Inorg. Chem. 48 (2009) 2181.
[8] M. Sadakane, T. Horiuchi, N. Kato, C. Takahashi, W. Ueda, Chem. Mater. 19 (2007) 5779.
[9] G. Zhang, Z. Zhao, J. Liu, G. Jiang, A. Duan, J. Zheng, S. Chen, R. Zhou, Chem. Commun. 46 (2010) 457.
[10] H. Laversin, D. Courcot, E.A. Zhilinskaya, R. Cousin, A. Aboukaïs, J. Catal. 241 (2006) 456.
[11] M. Haruta, T. Kobayashi, H. Sano, N. Yamada, Chem. Lett. 16 (1987) 405.
[12] G.J. Hutchings, J. Catal. 96 (1985) 292.
[13] M.C. Daniel, D. Astruc, Chem. Rev. 104 (2004) 293.
[14] T. Mitsudome, A. Noujima, Y. Mikami, T. Mizugaki, K. Jitsukawa, Angew. Chem., Int. Ed. 49 (2010) 5545.
[15] J.D. Stiehl, T.S. Kim, S.M. McClure, C.B. Mullins, J. Am. Chem. Soc. 126 (2004) 13574.
[16] X.W. Xie, Y. Li, Z.Q. Liu, M. Haruta, W.J. Shen, Nature 458 (2009) 746.
[17] M.S. Chen, D.W. Goodman, Chem. Soc. Rev. 37 (2008) 1860.
[18] M. Kotobuki, R. Leppelt, D.A. Hansgen, D. Widmann, R.J. Behm, J. Catal. 264 (2009) 67.

[19] N. Weiher, E. Bus, L. Delannoy, C. Louis, D.E. Ramaker, J.T. Miller, J.A. van Bokhoven, J. Catal. 240 (2006) 100.
[20] C.J. Jia, Y. Liu, H. Bongard, F. Schth, J. Am. Chem. Soc. 132 (2010) 1520.
[21] A.A. Hering, C.J. Kiely, A.F. Carley, P. Landon, G.J. Hutchings, Science 321 (2008) 1331.
[22] C. Harding, V. Habibpour, S. Kunz, A.N. Farnbacher, U. Heiz, B. Yoon, U. Landman, J. Am. Chem. Soc. 131 (2009) 538.
[23] G. Renaud, R. Lazzari, C. Revenant, A. Barbier, M. Noblet, O. Ulrich, F. Leroy, J. Jupille, Y. Borensztein, C.R. Henry, J. Deville, F. Scheurer, J. Mane-Mane, O. Fruchart, Science 300 (2003) 1416.
[24] W.C. Conner, J.L. Falconer, Chem. Rev. 95 (1995) 759.
[25] A. Caballero, J.P. Holgado, V.M. Gonzalez-delaCruz, S.E. Habas, T. Herranz, M. Salmeron, Chem. Commun. 46 (2010) 1097.
[26] T. Schalow, M. Laurin, B. Brandt, Angew. Chem. Int. Ed. 44 (2005) 7601.
[27] Y. Liu, C. Jia, J. Yamasaki, O. Terasaki, F. Schüth, Angew. Chem. Int. Ed. 49 (2010) 5771.
[28] Y. Wei, J. Liu, Z. Zhao, A. Duan, G. Jiang, C. Xu, J. Gao, H. He, X. Wang, Energy Environ. Sci. 4 (2011) 2959.
[29] Y. Wei, L. Jian, Z. Zhao, G. Jiang, A. Duan, H. He, X. Wang, Chin. J. Catal. 31 (2010) 283.
[30] Y. Wei, J. Liu, Z. Zhao, Y. Chen, C. Xu, A. Duan, G. Jiang, H. He, Angew. Chem. Int. Ed. 50 (2011) 2326.
[31] J. Liu, Z. Zhao, C. Xu, A. Duan, G. Jiang, Energy Fuels 24 (2010) 3778.
[32] G.N. Vayssilov, Y. Lykhach, A. Migani, T. Staudt, G.P. Petrova, N. Tsud, T. Skála, A. Bruix, F. Illas, V. Matolín, K.M. Neyman, J. Libuda, Nat. Mater. 10 (2011) 310.
[33] Z. Gu, R. Horie, S. Kubo, Y. Yamada, A. Fujishima, O. Sato, Angew. Chem. Int. Ed. 41 (2002) 154.
[34] R. Levy, N.T.K. Thanh, R.C. Doty, I. Hussain, R.J. Nichols, D.J. Schiffrin, M. Brust, D.G. Fernig, J. Am. Chem. Soc. 126 (2004) 10076.
[35] I. Ojea-Jomenez, V. Puntes, J. Am. Chem. Soc. 131 (2009) 13320.
[36] J.R. Ferraro, K. Nakamoto, Introductory Raman Spectra, Academic Press, New York, 1994.
[37] I.E. Wachs, J.M. Jehng, G. Deo, B.M. Weckhuysen, V.V. Guliants, J.B. Benziger, Catal. Today 32 (1996) 47.
[38] A. Martínez-Arias, M. Fernández-García, L.N. Salamanca, R.X. Valenzuela, J.C. Conesa, J. Soria, J. Phys. Chem. B 104 (2000) 4038.
[39] X. Lin, L. Li, G. Li, W. Su, Mater. Chem. Phys. 69 (2001) 236.
[40] P. Fang, M. Luo, J. Lu, S. Cen, X. Yan, X. Wang, Thermochim. Acta 478 (2008) 45.
[41] K. Krishna, A. Bueno-Lopez, M. Makkee, J.A. Moulijn, Appl. Catal. B 75 (2007) 201.
[42] Z. Zhao, Y. Yamada, A. Ueda, H. Sakurai, T. Kobayashi, Catal. Today 163 (2004) 93.
[43] G. Zhang, Z. Zhao, J. Xu, J. Zheng, J. Liu, G. Jiang, A. Duan, H. He, Appl. Catal. B 107 (2011) 302.
[44] S.Y. Liu, S.M. Yang, Appl. Catal. A 334 (2008) 92.
[45] S. Scire, S. Minico, C. Crisafulli, C. Satriano, A. Pistone, Appl. Catal. B 40 (2003) 43.
[46] J.B. Park, J. Graciani, J. Evans, D. Stacchiola, S. Ma, P. Liu, A. Nambu, J.F. Sanz, J. Hrbek, J.A. Rodriguez, Proc. Natl. Acad. Sci., USA 106 (2009) 4975.
[47] N. Russo, D. Fino, G. Saracco, V. Specchia, Catal. Today 137 (2008) 306.
[48] C. Ma, Z. Mu, J. Li, Y. Jin, J. Cheng, G. Lu, Z. Hao, S. Qiao, J. Am. Chem. Soc. 132 (2010) 2608.
[49] Q. Fu, H. Saltsburg, M. Flytzani-Stephanopoulos, Science 301 (2003) 935.
[50] D.A. Bulushev, I. Yuranov, E.I. Suvorova, P.A. Buffat, L. Kiwi-Minsker, J. Catal. 224 (2004) 8.
[51] X. Zhang, A. Corma, Angew. Chem. Int. Ed. 47 (2008) 4358.
[52] M. Turner, V.B. Golovko, O.P.H. Vaughan, P. Abdulkin, A. Berenguer-Murcia, M.S. Tikhov, B.F.G. Johnson, R.M. Lambert, Nature 454 (2008) 981.
[53] E. Bêche, P. Charvin, D. Perarnau, S. Abanades, G. Flamant, Surf. Interface Anal. 40 (2008) 264.
[54] M.M. Natile, A. Glisenti, Chem. Mater. 17 (2005) 3403.
[55] J. Guzman, B.C. Gates, J. Am. Chem. Soc. 126 (2004) 2672.
[56] M.M. Schubert, S. Hackenberg, A.C. Van Veen, M. Muhler, V. Plzak, R.J. Behm, J. Catal. 197 (2001) 113.
[57] P. Fornasiero, J. Kaspar, M. Graziani, J. Catal. 167 (1997) 576.
[58] Y. Azizi, C. Petit, V. Pitchon, J. Catal. 269 (2010) 26.
[59] J. Liu, Z. Zhao, J. Lan, C. Xu, A. Duan, G. Jiang, X. Wang, H. He, J. Phys. Chem. C 113 (2009) 17114.
[60] J.P.A. Neeft, W. Schipper, G. Mul, M. Makkee, J.A. Moulijn, Appl. Catal. B 11 (1997) 365.
[61] Z. Ma, S.H. Overbury, S. Dai, J. Mol. Catal. A 273 (2007) 186.
[62] K. Hinot, H. Burtscher, A.P. Weber, G. Kasper, Appl. Catal. B 71 (2007) 271.
[63] Z. Zhang, Y. Zhang, Z. Wang, X. Gao, J. Catal. 271 (2010) 12.